Thesis for the Degree of Doctor of Philosophy

Silicon nitride-based integrated components for optical communication

Alexander Caut

CHALMERS

Photonics Laboratory
Department of Microtechnology and Nanoscience - MC2
Chalmers University of Technology
Göteborg, Sweden, 2023

Silicon nitride-based integrated components for optical communication
Alexander Caut
Göteborg, November 2023

ISBN 978-91-7905-954-5
Doktorsavhanlingar vid Chalmers tekniska högskola,
Ny serie nr 5420
ISSN 0346-718X

Photonics Laboratory
Department of Microtechnology and Nanoscience (MC2)
Chalmers University of Technology
SE-412 96 Göteborg
Sweden
Phone: +46 (0)76-422 54 97

Printed in Sweden by
Reproservice
Chalmers tekniska högskola
Göteborg, Sweden, November 2023

Silicon nitride-based integrated components for optical communication
Alexander Caut
Photonics Laboratory
Department of Microtechnology and Nanoscience - MC2
Chalmers University of Technology

Abstract

To follow the trend of the data traffic and to limit the size of the hyperscale data centers, communication solutions offering small footprint, low cost and low power consumption are needed. Optical interconnects used in data centers are mostly short reach (approximately 100 m) based on GaAs-based 850 nm vertical-cavity surface emitting lasers (VCSELs) and OM4 multimode fibers (MMF). However, with 1 km-long optical links, the use of VCSEL-MMF at 850 nm becomes challenging at high data rates (Tb/s) due to large modal dispersion and high propagation loss. Therefore, other cost-effective methods are needed to compensate these limits. Single mode GaAs-based VCSELs have been demonstrated at 1060 nm of wavelength, where the chromatic dispersion is lower, for optical links ranging between 300 m and 10 km. This solution could be a better alternative than InP-based distributed feedback laser sources at 1310 nm in terms of cost and energy dissipation. As the modulation bandwidth of GaAs-based single mode VCSELs is limited to around 30 GHz, reaching the capacity target then requires a wavelength division multiplexing scheme with parallel single-core fibers (SCFs) or even multi-core fibers (MCFs)

In this thesis we discuss different types of demultiplexers at 1060 nm of wavelength. The proposed designed demultiplexers are arrayed waveguide gratings (AWGs) and cascaded Mach-Zehnder interferometers (MZIs). These two technologies are compared in terms of transmission, bandwidth, crosstalk and footprint with the number of output channels. Grating couplers at 1060 and 850 nm for on-chip coupling are also studied. The goal is to couple the light coming from a single mode fiber or a VCSEL with the lowest possible loss and back reflection.

Keywords: arrayed waveguide gratings, Mach-Zehnder interferometers, insertion loss, crosstalk, grating couplers, power splitters, polarization, silicon photonics, silicon nitride.

Publications

This thesis is based on the work contained in the following papers:

[A] **Alexander Caut**, Marcello Girardi, Victor Torres-Company, Anders Larsson, and Magnus Karlsson, "Channel Scalability of Silicon Nitride (De-)multiplexers for Optical Interconnects at 1 μm", in *Journal of Lightwave Technology (JLT)*, 2023.
DOI: 10.1109/JLT.2023.3306478

[B] Mehdi Jahed, **Alexander Caut**, Jeroen Goyvaerts, Marc Rensing, Magnus Karlsson, Anders Larsson, Gunther Roelkens, Roel Baets, and Peter O'Brien, "Angled Flip-Chip Integration of VCSELs on Silicon Photonic Integrated Circuits", in *Journal of Lightwave Technology (JLT)*, Vol. 40, No. 15, pp. 5190-5200, August 1, 2022.
DOI: 10.1109/JLT.2022.3172781

[C] **Alexander Caut**, Vijay Shekhawat, Victor Torres-Company, and Magnus Karlsson, "Polarization-insensitive silicon nitride photonic receiver at 1 μm for optical interconnects", *Submitted for publication, 2023*

[D] **Alexander Caut**, Victor Torres-Company, and Magnus Karlsson, "Receiver platform based on thin Silicon Nitride waveguides at 1 μm", *Submitted for publication, 2023*

[E] Marcello Girardi, Òskar B. Helgason, **Alexander Caut**, Magnus Karlsson, Anders Larsson, and Victor Torres-Company, "Multilayer integration in silicon nitride: decoupling linear and nonlinear functionalities for ultralow loss photonic integrated systems", in *Optics Express*, Vol. 31, No. 19, 11 Sep 2023.

Other publications by the author, not included in this thesis, are:

[F] A. S. Alam, M. Girardi, **A. Caut**, A. Larsson, V. Torres-Company, M. Galili, Y. Ding, and K. Yvind, "LiNbO3/Si3N4-Bilayer Vertical Coupler for Integrated Photonics", *CLEO 2020*

[G] Marcello Girardi, Òskar B. Helgason, **Alexander Caut**, Magnus Karlsson, Anders Larsson, and Victor Torres-Company, "3D Integration of Microcombs", *CLEO 2023*

[H] Hezhi Zhang, Ching-Wen Shih, Denis Martin, **Alexander Caut**, Jean-François Carlin, Raphaël Butté and Nicolas Grandjean, "Short cavity InGaN-based laser diodes with cavity length below 300 μm", in *Semiconductor Science and Technology*, 34, 2019

[I] Hezhi Zhang, Ching-Wen Shih, Denis Martin, **Alexander Caut**, Jean-François Carlin, Raphaël Butté, and Nicolas Grandjean, "Broadened Bandwidth Amplified Spontaneous Emission from Blue GaN-Based Short-Cavity Superluminescent Light-Emitting Diodes", in *ECS Journal of Solid State and Technology*, 2020, 9 015019

Contents

Acknowledgement

First of all, I would like to thank Professor Magnus Karlsson for giving me the opportunity to experience this adventure in the photonics laboratory, for guiding me all the way to my doctorate and for always keeping the door open when I had something to clarify in the course of my research. I would like to thank my co-supervisor, Professor Victor Torres-Company, for the exceptional inspiration he has given me throughout these years.

I would like to thank Dr Marcello for the work he did and the time he spent in the cleanroom making my components. I would like to thank Dr Krishna Sundar Twayana for his advice during my initial characterization phases.

I would like to thank Muhammad Bilal Aziz, Rasmus Larsson, Dr. Ali Mirani, Dr. Kovendhan Vijayan, Dr. Jochen Schröder and Prof. Peter Andrekson for their support in the preparation of the laboratory exercises in order to provide quality work to the students enrolled in the fiber optical communication course.

I am particularly greatful to Jeanette Träff for helping me in my first few days in Sweden. I am also thankful to Gunnel Berggren for giving me weekly diaries to improve my Swedish.

François-Marie Arouet dit Voltaire (1694-1778) once said that "Homeland is where you live happily", so I'd like to thank all my friends in Gothenburg who have made Sweden my new home. Among them Fredrik, Albin, Marwan and Birk.

I also would like to thank Austėja for her support and for the beautiful walks around Gothenburg.

I would like to thank my high school teacher Dr. Emmanuel Vesin for passing on to me his vocation for Physics and I express my gratitude to my CPGE Physics professor Anne Guibé for her teachings and passing on her rigor in the subject.

Last but not least, my deepest thanks go to my family. I want to express my profound gratitude to my parents for their support during my PhD journey. I am also grateful to my little sister Chloé for bringing me joy through my research and for sharing her passions and thoughts.

Alexander Caut

Göteborg, November 2023

Acronyms

AWG	arrayed waveguide grating
MZI	Mach-Zehnder interferometer
GC	grating coupler
SMF	single-mode fiber
MMF	multi-mode fiber
CWDM	coarse wavelength-division multiplexing
DWDM	dense wavelength-division multiplexing
SNR	signal-to-noise ratio
BER	bit error rate

CHAPTER 1

Introduction

1.1 Network traffic

Global data traffic has been increasing at an exponential rate in the past decade. Mobile data traffic alone was 62 exabytes per month in 2020 and is expected to reach 607 exabytes in 2025 and 5016 in 2030 [1, 2]. While 5G technology is being released worldwide, 6G is already under development to meet the high demand for high-speed internet [2] and the backbone of the internet infrastructure are optical cables and data centers. Data centers consist of a vast amount of servers where most of the world's data is stored and accessed. These servers require a substantial amount of power and cooling. According to an European Commission report, data centers consumed 2.7 % of electricity within the EU in 2018 and could reach 3.21 % in 2030 [3]. This is due to the growing size and number of data centers. The number of hyperscale data centers was 259 in 2015, 448 in 2018 and reached 700 at the end of 2021 [4]. The largest data center measures now 1 000 000 m^2 [5]. This means that to limit the increasing size of the hyperscale datacenters, interconnect solutions offering small footprint, low cost and low power consumption will be needed. Today's optical interconnects used in data centers are short reach and use standard GaAs-based 850 nm vertical-cavity surface emitting lasers (VCSELs) and OM4 multimode fibers (MMFs) [6–8]. At this wavelength, the fiber links typically reach distances of 100 m [9] at data rates of 25 Gb/s on-off keying (OOK) and 50 Gb/s pulse amplitude modulation 4-level (4PAM) [8, 10, 11]. 4PAM modulation is of interest as the data rate is increased by a factor of 2. However, the 4-PAM modulation format requires a higher signal-to-noise ratio (SNR) to get the same level of bit error rate (BER) than with OOK modulation [11].

1.2 VCSEL-based interconnects

1.2.1 Short-reach interconnects at 850 nm

GaAs-VCSELs at 850 nm are used in 95% of optical interconnects with typical lengths around 100 m [9, 12]. Data rates close to 100 Gb/s were achieved on these VCSELs with 4PAM [13]. Typical energy dissipations close to 100 fJ/bit at 50 Gb/s are reported in Ref [14]. However, the length of the optical links are limited due to chromatic dispersion in the fiber and propagation loss. The chromatic dispersion at 850 nm reaches -85 ps/nm/km in silica MMF and the propagation loss exceeds 2 dB/km [7, 15]. One possibility to reduce the chromatic dispersion effect consists in using single-mode (SM) VCSELs as the bandwidth is much narrower than for multimode ones [7]. Moreover, SM-VCSELs reduce the impact of modal dispersion if launched into carefully selected mode groups of the MMF [7, 16]. Unfortunately, this also requires higher alignment precision as misalignment between SM-VCSELs and MMFs can lead to higher order modes excitation [7].

1.2.2 Medium-reach interconnects at 1060 nm

With the increasing size of hyperscale data centers and the limited length of short links at 850 nm, new solutions are needed to face this challenge. With the recent development of efficient GaAs SM-VCSELs emitting at 1060 nm [17] and with the reduced propagation loss and chromatic dispersion at 1060 nm (about 1 dB/km and -25 ps/nm/km respectively) [15], optical links at 1060 nm are of interest. After several efforts, with a pre-emphasis on GaAs-VCSELs at 50 Gb/s an error-free VCSEL-SMF 1-km long optical link was achieved without forward error correction (FEC) [18]. The used SMF was a prototype with negative dispersion. Links using InP distributed feedback lasers at 1310 nm are another alternative due to low propagation loss and chromatic dispersion but less efficient [8].

1.2.3 Space division multiplexing (SDM)

To enable high data rate transmission, one existing technology based on multicore fibers (MCFs) consists of transmitting the data from an array of VCSELs, spatially matching the different cores of the fiber. According to Ref [19], the record demonstrated in SDM systems in 2020 was 10000 Tb/s. However, the spectral efficiency of this type of fiber is limited by the core count due to crosstalk coming from adjacent cores [19].

1.2.4 Wavelength division multiplexing (WDM)

WDM is another technology to reach high data rates. The two main types of WDM are coarse WDM (CWDM) where the channel spacing is usually 20-25 nm [20, 21] and dense WDM (DWDM) where the channel spacing is below 1 nm [22]. DWDM is the preferred scheme for long-haul communications in the C band (1530-1565 nm) due to the limited bandwidth of erbium doped fiber amplifiers (EDFAs). With the reduced footprint of VCSELs (250 x 250 μm^2) [20], it is possible to combine signals coming from different VCSELs (emitting at different wavelengths) into one fiber with the help of a multiplexer (MUX). Schemes using shortwave WDM that multiplex four wavelengths (850, 880, 910 and 940 nm) in a multimode fiber OM5 have been demonstrated in Ref [23, 24] with 4PAM modulation and enable up to 400 Gb/s [25]. However, parallel discrete VCSELs increase the footprint of the transmitter where there is a need for higher bandwidth densities. One solution to reduce the footprint consists in manufacturing multi-wavelength VCSELs arrays as proposed in Ref [8].

1.2.5 Role of silicon photonics

The technologies mentioned above allow a significant increase of the data rate in optical links, but with the substantial lack of space in the optical interconnects, the need of small device footprint and high bandwidth density require low cost and integrated solutions for space and wavelength division multiplexing.

On the one hand, electronic integrated circuits (EICs) are currently widespread in telecommunication and silicon is one of the dominating materials in the electronic market due to its properties, abundance and compatibility with CMOS processes. On the other hand, photonic integrated circuits (PICs) are also of interest for CMOS compatible wafers. Silicon photonics is also well established in the market due to its low cost and its CMOS-compatibility. For example, IBM is developing low-cost hybrid silicon electronic-photonic chips for high bandwidth transmission (10 Tb/s) [26]. In addition, according to Ref [27], silicon photonics is playing a key role in future generations co-packaging technology. To enable significant tighter integration between optical links and electronic integrated circuits, integration of lasers and electronics is essential. However, due to the indirect bandgap of silicon, electron-hole radiative recombination that is necessary to create stimulated emission cannot to occur. This is why semiconductor lasers are based on direct bandgap materials, typically in the III-V semiconductor region [28, 29].

One cost-effective technique used to integrate light sources such as VCSELs in PICs is to flip-chip bond the laser over the PIC with an optimized tilt-angle into a surface coupler. Flip-chip integration of VCSELs have been demonstrated previously in Ref [30] and is also discussed in Paper [B]. The flip-chip is realized with deposition of a solder ball between the VCSEL and the PIC, also allowing electrical contacting. Moreover, integration of laser sources via direct hetero-epitaxial growth of III-V materials on silicon have been demonstrated [31] and co-packaging of electronic and PICs led to recent demonstrations of 1.6 Tb/s transceivers [32]. In addition, silicon photonics enables compact and low cost integration of WDM components while being compatible with complementary metal-oxide-semiconductor (CMOS) processes [33]. For example, the arrayed waveguide grating (AWG) is a well known component for WDM [34–36] and can be integrated in silicon [22], silicon nitride [20], silica [37] and other materials.

1.3 This thesis

This thesis will first discuss in Chapter 2 the different usable materials for the integrated optical waveguides, the simulation methods to estimate the insertion loss and also the different waveguide designs. The focus of this thesis is on design, characterization and analysis of different types of fiber-chip couplers at 850 nm and 1060 nm. Chapter 3 of the thesis will focus on the transmitter side of the WDM optical interconnect at 1060 nm. Paper [A] expands the results of Chapter 3 and proposes two types of (de-)multiplexers which are (i) the arrayed waveguide gratings (AWGs) and (ii) the cascaded Mach-Zehnder interferometers (MZIs). A deep analysis on robustness of these two technologies to fabrication deviations (waveguide dimension, refractive index change), crosstalk, insertion loss, signal-noise-ratio (SNR), device's footprint with the number of channels and sensitivity to temperature compared to the VCSEL's temperature shift is presented as well. Chapter 4 will focus on grating couplers and a photonic integrated circuit including a flip-chipped VCSEL and a photodiode at 850 nm is demonstrated on Paper [B]. Chapters 5 will then focus on the receiver of the optical interconnect at 1060 nm. Papers [C] and [D] expands the results of Chapter 5 on the receiver at 1060 nm and focus on polarization insensitivity. Paper [C] proposes a receiver based on a square polarization independent waveguide and Paper [D] a receiver based on a thin waveguide. Chapter 6 proposes a photonic integrated circuit design based on micro-comb frequency source for optical interconnects at 1550 nm. The explored demultiplexers in this chapters are AWGs and a demonstration of a photonic integrated circuit is shown in Paper [E]. Finally, Chapter 7 presents an outlook for future work on these optical interconnects and Chapter 8 summarizes the main results in the papers.

CHAPTER 2

Waveguide theory and simulation methods

Design of integrated photonic devices requires selection of the appropriate material and the waveguide geometry depending on the wavelength and the device requirements. Indeed, the waveguide material will have an impact on the mode confinement, the device's footprint and the waveguide dimensions. The waveguide is either sandwiched between cladding layers made of silica for good mode confinement or just deposited on top of a silica cladding layer. For good mode confinement, the core index must be larger than the cladding index. The most commonly used waveguide materials in silicon photonics are silicon, silicon nitride and silica, and these will be discussed below.

2.1 Waveguide materials

2.1.1 Silicon waveguides

Silicon (Si) is a material that is CMOS-compatible, which is important for semiconductor devices. Due to high refractive index contrast between silicon and silicon dioxide (SiO_2), the mode confinement in the waveguide is excellent, allowing ultra-short bending radius (a few micrometers) and thus small footprint. However this also leads to strong roughness of waveguide sidewalls and higher scattering loss [38]. Si-waveguides are mostly based on a silicon-on-insulator (SOI) platform. In addition, the Si material has low absorption in the wavelength range 1.1-8.5 μm, which means this material cannot be used for optical interconnects with wavelengths shorter than 1.1 μm (for example 850 nm or even 1060 nm) [39]. Finally, Si waveguides have an effective index that is very sensitive to waveguide width variation. Indeed, multiplexers (AWGs, MZIs) made of Si waveguides show a shift of 1 nm in the transmission spectra for a waveguide width deviation of 1 nm [39]. As we want to make robust designs to any fabrication deviation, this material is therefore less suitable for our devices.

2.1.2 Silicon nitride waveguides

Silicon nitride (SiN) waveguides make a good alternative to waveguides made of silicon. Also being a CMOS-compatible material, the refractive index of Si_3N_4 being around 2.00 at 1050 nm of wavelength, the refractive index contrast between the SiO_2 cladding and the waveguide is thus much smaller. This decreases the sensitivity of scattering loss due to sidewall roughness. Silicon nitride can be deposited either in low-pressure chemical vapor deposition (LPCVD) at 700°C, in plasma enhanced chemical vapor deposition (PECVD) at less than 400°C [38,40] and also with sputtering. The LPCVD deposition method has the advantage of keeping control of the SiN stoichiometry and is most suited for the telecom band (1550 nm) [38], and also in the 1 μm band. Moreover, SiN can be used for wavelengths much shorter than 1.1 μm as opposed to Silicon, and varying the N/Si ratio can cover wavelengths close to 400 nm [39]. The SiN waveguide is deposited with LPCVD in Paper [A] and PECVD in Paper [B] (at 850 nm of wavelength). The drawback of SiN with respect to Si is that its lower refractive index leads to lower mode confinement, which prevents small bending radius in curved waveguides and increases the device's footprint [41]. However, this is largely compensated by the ultra-low propagation loss obtained in SiN waveguides, which is an important priority for our research. Therefore, SiN was selected for fabrication in the cleanroom and platform development.

2.1.3 Silica waveguides

Silica (SiO_2) is another interesting alternative to silicon for wavelengths shorter than 1.1 μm. Due to low index contrast between the core and the cladding (also made of silica), the waveguide dimensions can almost match the fiber's core, enabling ultra low fiber-chip coupling loss (0.1 dB) [39]. In addition, this material can provide low propagation loss

(0.017 dB/cm for a 7 μm x 7 μm waveguide) [39]. Nevertheless, the extremely low contrast between the core and the cladding will require ultra-large bending radii (up to tens of millimeters) and thus to large size devices [39, 41].

2.2 Waveguide geometries

2.2.1 Designs

The most common waveguide for telecommunication is the optical fiber which consists of a circular core made of silica surrounded by a circular silica cladding. The relative refractive index difference between the core and the cladding is circa 0.01, the core index being greater than the cladding index. However, for optical integration, the waveguide geometry needs to be adapted to the layer deposition which is planar. Therefore, the preferred geometry in integrated photonics is rectangular and the main waveguide designs are the strip and the rib waveguides [42] as illustrated in figure 2.1. The core materials used were discussed in the previous section (silicon nitride is chosen here) and the cladding is silica. Thick and wide waveguides surrounded by cladding allow strong confinement of the optical mode in both vertical and horizontal directions.

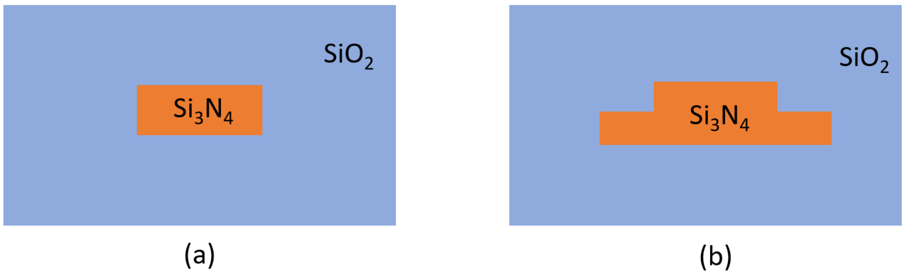

Figure 2.1: Scheme of (a) strip and (b) rib waveguide.

The strip waveguide requires only one etching step whereas the rib waveguide requires two steps [43]. Moreover, the strip geometry allows smaller bending radius, which reduces the device footprint. However, the main source of propagation losses is the roughness on the waveguide sidewalls and the rib design has lower sidewalls compared to the strip design for the same geometry [43]. This makes the rib design interesting for devices based on thick waveguides (740 nm thick for SiN at 1550 nm of wavelength). The waveguide confinement factor represents how well the electromagnetic field is confined in the core and can be defined as the ratio of the electromagnetic fields within the core area to the electromagnetic fields within the full structure (top and bottom claddings included) [44–46]. Therefore, a thick waveguide will have a larger confinement factor than a thin waveguide.

2.2.2 Mode propagation and polarizations

The guided mode in the waveguide has a parameter called effective index denoted n_{eff}, given by

$$n_{eff} = \frac{\beta}{k_0}, \tag{2.1}$$

where β is the waveguide propagation constant and $k_0 = \frac{2\pi}{\lambda_0}$ the wavenumber with λ_0 being the wavelength of light in vacuum. The condition on the effective index for the optical mode to be guided in the waveguide is $n_{cl} < n_{eff} < n_c$, n_{cl} being the cladding index and n_c the core index. Fig. 2.2 shows an example of the simulated mode field profiles in the two polarization states (in the case of a single mode waveguide at 1550 nm of wavelength). The waveguide in the simulation is SiN and the cladding is SiO_2. There are two polarization states possible for the mode field: the TE polarization state in which the electric field is in the y-direction (fig. 2.2.a) and the TM polarization state in which the electric field is in z-direction (fig. 2.2.b).

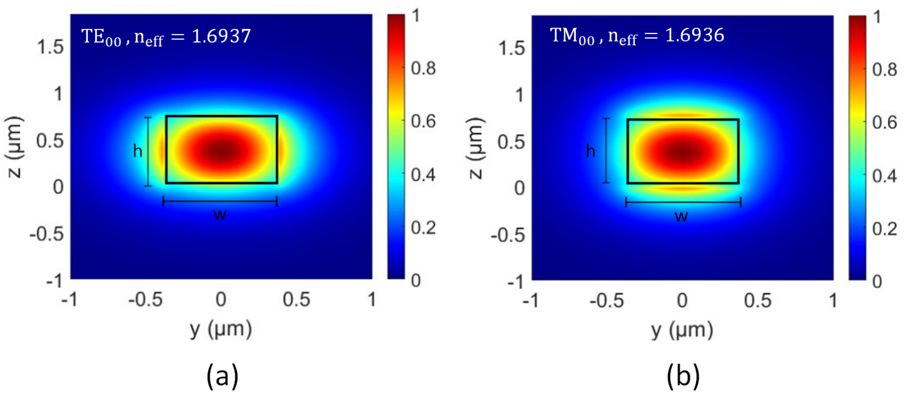

Figure 2.2: Mode field profiles of (a) TE_{00} and (b) TM_{00} modes (h = 740 nm, w = 740 nm) at 1550 nm of wavelength.

The waveguide is square-shaped and is 740 nm thick and 740 nm wide. Therefore the fundamental TE and TM modes have almost the same effective indices ($n_{\text{eff, TE00}} = 1.6937$ and $n_{\text{eff, TM00}} = 1.6936$). The simulations are carried out in lumerical FDE (Finite Difference Eigenmode). Even though the waveguide is square-shaped, the effective indices of the TE_{00} and TM_{00} slightly differ due to the anti-symmetry of the simulation region. Indeed, the different layers of SiO_2 (thermal, LPCVD and PECVD) are also taken in account, each one having slightly different refractive indices. As the modes are well confined in thick waveguides, low bending radius can be achieved with low loss. In addition, thick waveguides can achieve low polarization sensitivity as shown in the simulations. However, thick waveguides need to have a reduced width in order to be single mode. As a result, the modes shown in Figure 2.2 have a strong interaction with the sidewalls, leading to higher radiation loss due to roughness [47]. One possibility to reduce the mode interaction with the sidewalls consists in increasing the waveguide's width. Unfortunately, the waveguide would become multimode as higher-order modes can be excited [48] and propagate through the cascaded devices in a photonic integrated circuit, thus spoiling the signal. Therefore, there is a tradeoff between good mode confinement and single mode behaviour. Fig. 2.3 shows the simulation of the mode field profiles for a 200 nm thick and 1500 nm wide waveguide, at the same wavelength.

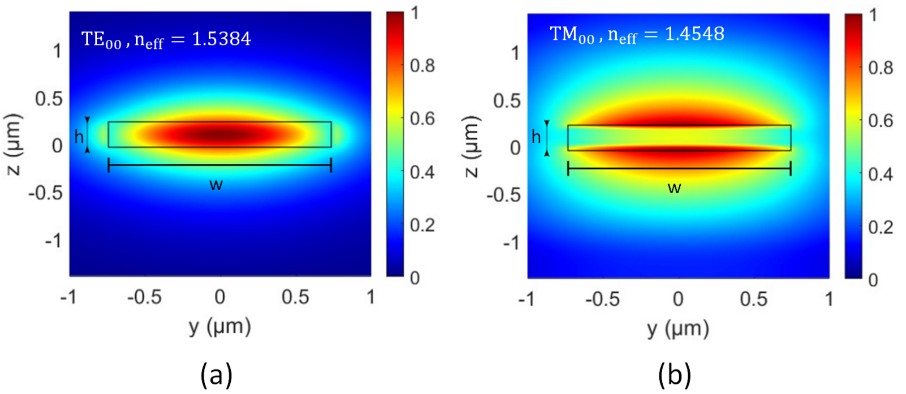

Figure 2.3: Mode field profiles of (a) TE_{00} and (b) TM_{00} modes (h = 200 nm, w = 1500 nm) at 1550 nm of wavelength.

The simulations show that mode confinement is more moderate when looking at the effective index values. The fundamental TE_{00} mode is more confined than the TM_{00} mode ($n_{eff,\ TE00} = 1.5384 > n_{eff,\ TM00} = 1.4548$). As the waveguide is thin and rectangular-shaped, the modes are much less confined than in the square-shaped waveguide in fig. 2.2. This generally results in higher radiation losses in bent waveguide sections which have to be compensated with larger bending radius (thus increasing the size of the device). As the TE mode is more confined than the TM mode and thus less lossy, this is why the TE polarization state is preferred in integrated optics.

In the next chapters, the fabricated devices we are going to explore will be based on thin waveguides (around 160-170 nm thick and 900 nm wide) and a center wavelength around 1035 nm.

2.3 Simulation methods

This section introduces the different simulation methods (FDTD, varFDTD and EME) and explains which method is the most suitable depending on the optical device.

2.3.1 FDTD solver

The FDTD solver simulates the whole device by solving the Maxwell equations on a discrete spatial and temporal grid. The entire structure is divided into multiple cells and the different field components (Ex, Ey, Ez, Hx, Hy and Hz) are solved for each cell. It can simulate 3D photonic structures such as grating tapers, tapers, Y-splitters and multimode interferometers (MMIs). However, the computing time increases exponentially with the size of the device. Therefore this solver is used to simulate small devices in 3 dimensions (typical size: 20 μm x 40 μm x 1.5 μm) such as grating couplers, or other devices with bent structures (Y-splitters, directional couplers). Finally, the simulation accuracy and computation time are increased when reducing the size of the cells.

2.3.2 varFDTD solver

The varFDTD solver basically collapses a 3D-FDTD simulation into an efficient 2D-FDTD simulation (often referred as 2.5D-FDTD), thus significantly reducing memory requirements and computing time compared to pure FDTD. This solver can thus simulate much bigger devices than a conventional 3D-FDTD simulation (size: 1000 μm x 400 μm). However, this method assumes that there is no coupling between the slab modes guided in the vertical waveguide structure, or no polarization conversion [49]. Thus this method is efficient for planar and wide structures. Typical devices that can be simulated with varFDTD are as ring resonators, multi-mode interferometers (MMIs), directional couplers (DCs) or Mach-Zehnder interferometers (MZIs). Nevertheless, convergence testings are necessary to increase the simulation accuracy and, depending on the size of the device, careful checks can be made with either 3D-FDTD or EME simulations for result verifications.

2.3.3 EigenMode Expansion (EME) solver

EME is a frequency domain method that consists in bi-directionally propagating the device to calculate the final S matrix. This simulation method is adapted for straight continuously varying structures such as tapers or MMIs. The first step of the EME solver consists in dividing the device structure in a set of cells. Then the solver requires the selection of the number of propagating modes for each defined section of the device. Finally, the propagating mode for each input/output port of the device are bi-directionally propagated through the device. The first advantage of the EME solver over FDTD is that it only needs one cell to simulate a rectangular region (for example the rectangular region of the MMI). The second advantage is when in analysis mode, the solver can scan the length of a tapered structure with hundreds of simulations in a few minutes. For comparison, this step with FDTD would take several hours to realize only a few simulations. In analysis mode, the solutions to each section is bi-directionally propagated to calculate the S matrix of the entire device. This method is extremely efficient as it allows the calculation of the optimal length of the device. To increase the simulation accuracy, the number of propagating modes needs to be increased.

	Grating coupler	MMI	Directional coupler	MZI
FDTD	4 min(2D), 2 h(3D)	1 h	1 h	60 h
varFDTD	N.A.	4 min	4 min	30 min
EME	N.A.	$<$ 4 min	N.A.	N.A.

Table 2.1: Solvers running times for different kind of devices

2.3.4 Summary

The running time of the different solvers and a few example devices are summarized in table 2.1. The grating coupler, MMI, directional coupler and the MZI have a size of respectively: 16 μm x 35 μm, 8 μm x 110 μm, 80 μm x 200 μm (bent waveguides included) and 700 μm x 200 μm. Concerning the MMI, the EME solver will find the optimal length of the rectangular region much faster than the other methods.

CHAPTER 3

Demultiplexing technologies for coarse wavelength-division multiplexing (CWDM)

In this chapter is proposed an integrated solution for future optical interconnects at 1060 nm. Different demultiplexing technologies are reviewed and based on manufacturing tolerance and performance, two are selected for the study in Paper [A]: the arrayed waveguide grating (AWG) and the cascaded Mach-Zehnder interferometer (MZI). This chapter then presents the design steps of the chosen technologies.

3.1 An integrated solution based on space and wavelength division multiplexing

To face the increasing demand for high interconnect capacity, the key challenge is reaching a capacity of several Tb/s [50]. In Paper [A] we propose an integrated solution based on short reach coarse wavelength-division multiplexing (CWDM) at 1060 nm. Parallel single-core fibers (SCFs) or even multi-core fibers (MCFs) [51, 52] are used to reach the target capacity as illustrated in Figure 3.1.

Figure 3.1 shows multi-wavelength GaAs-based VCSEL arrays flip-chipped over grating couplers on a photonic integrated circuit (PIC). The VCSELs are single-mode and their polarization needs to be stably aligned with the grating coupler [17, 53]. Moreover, the flip-chipped

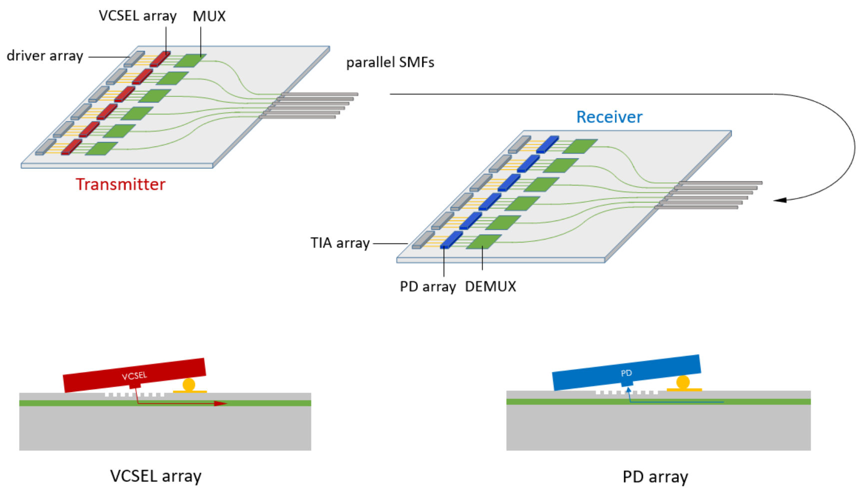

Figure 3.1: Short reach CWDM at 1060 nm. The light from the VCSEL array is coupled through grating couplers and guided to a multiplexer (MUX), a demultiplexer (DEMUX) and to an array of photodiodes (PD).

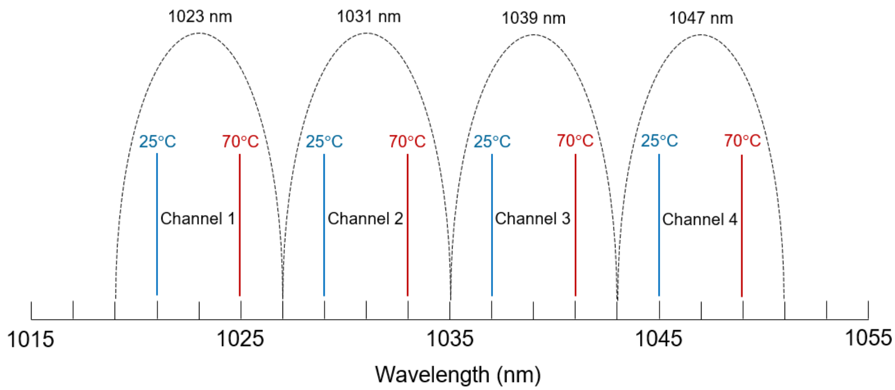

Figure 3.2: Channel allocation of the CWDM. The vertical dashed lines illustrate the wavelength emission of the VCSELs at different temperatures. As the VCSELs are sensitive to temperature changes, the bandwidth of the channels need to be broadband enough to avoid extra-loss.

VCSELs are tilted to ensure low optical feedback [53]. The channel separation between the VCSELs here is set to 8 nm. The VCSELs are emitting at center wavelengths 1023, 1031, 1039 and 1047 nm and Figure

3.2 shows the desired channel allocation for the CWDM. The light from the VCSELs reaching the photodiode (PD) is coupled with a grating coupler for each channel. As explained in chapter 2 of the thesis, silicon would allow compact integration of the passive components due ot its high refractive index (around 3.57 at 1060 nm), but it is not transparent in the 1015-1075nm spectral range [39, 54]. Therefore, the platform is made of silicon nitride (SiN). Finally, since the VCSEL's polarization are controlled, the transmitter is specifically designed for TE polarization. However, at the receiver side the polarization is no longer controlled as it is not maintained over distance in the parallel SMFs. Therefore, the receiver needs to be polarization independent, which is going to be discussed in chapter 5.

3.2 Bit error rate (BER) and power budget

In Ref [8] also at 1060 nm, the BER was calculated at the receiver when using two different modulation formats: on-off keying (OOK) and 4PAM at 25 Gbaud. To reach a maximum BER of 10^{-3} for hard decision forward error correction (FEC) [55], we estimated that the minimum power required was -14 dBm with OOK and -8 dBm with 4PAM. A power budget for each component (VCSEL-grating coupler, MUX, waveguide-fiber coupler, fiber-waveguide coupler, DEMUX, grating coupler-PD) was set based on the power received using 4PAM modulation format and a maximum insertion loss of 2 dB per component was estimated doable (Table 3.1).

The minimum desired data rate with this setup is 1 Tb/s. This is possible by multiplexing the 4 wavelengths of the VCSEL arrays to 6 parallel single-mode fibers in a single optical cable, where each VCSEL provides a data rate 50 Gb/s using 4PAM modulation format [8]. Therefore, with a single 4-array of VCSELs providing 200 Gb/s, a number of 6 arrays would provide 1.2 Tb/s.

The bit error rate (BER) for OOK is given by [56]:

$$\mathrm{BER} = \frac{1}{2}\mathrm{erfc}\big(\sqrt{\mathrm{SNR}_{\mathrm{tot}}}\big), \tag{3.1}$$

where $\mathrm{SNR}_{\mathrm{tot}}$ is the total signal-to-noise ratio (SNR) that includes the crosstalk XT and is expressed as:

$$\mathrm{SNR}_{\mathrm{tot}} = \Big(\frac{1}{\mathrm{SNR}} + \mathrm{XT}\Big)^{-1}. \tag{3.2}$$

	Loss (dB)	Power (dBm)
VCSEL output		6
Grating coupler	2	4
MUX	2	2
Waveguide-fiber	2	0
Fiber-waveguide	2	-2
DEMUX	2	-4
Grating coupler	2	-6

Table 3.1: Power budget for each component. The VCSELs can deliver 6 dBm of power [8].

We estimated with equation 3.2 that a crosstalk of -20 dB would give around a 1 dB-penalty on the SNR at a BER of 10^{-9}. Therefore, the maximum crosstalk value we would like for our devices is -20 dB. The crosstalk is analyzed for the AWGs and MZIs when increasing the number of channels. The average crosstalk per channel was calculated for each device for 4, 8 and 16 channels and the results are given in Paper [A].

3.3 Types of wavelength division (de-)multiplexers

In this section, we will review different types of demultiplexers. Their insertion loss, crosstalk level, fabrication tolerance and footprint will be discussed. Then we will explain which devices were selected for CWDM at 1 μm of wavelength.

3.3.1 Arrayed waveguide gratings

An AWG consists of a set of arrayed waveguides connecting two free propagation regions (FPRs), input waveguides linked to the first FPR and output waveguides to the second as shown in Figure 3.3. AWGs are attractive due to their potentially small footprint and to the low insertion loss and low crosstalk level they can provide.

The arrayed waveguides connecting the FPRs have a constant length increment. The light coming from the first FPR propagates through the arrayed waveguides in which each wavelength undergoes a phase shift provided by this length increment. The phase shift $\Delta\Phi_n$ of the n^{th} arrayed waveguide is linearly dependent on the frequency ν and is given by $\Delta\Phi_n = 2\pi n_c \nu l_n / c$, where c is the speed of light in vacuum, n_c the effective index of the arrayed waveguides and l_n the length of the n^{th} arrayed waveguide. Finally, the wavelengths will interfere constructively in the second FPR and focus at the output waveguides. The free spectral range (FSR) is set by the length difference between the arrayed waveguides [36]. In addition, the receiver and arrayed waveguide separations and the FPR length set the channel spacing [36].

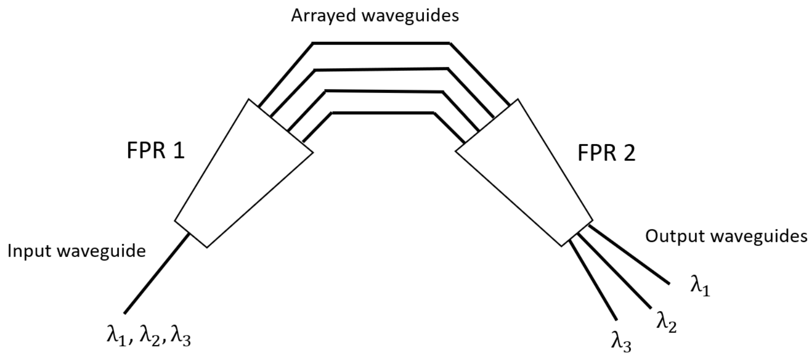

Figure 3.3: Illustration of an AWG

One particular advantage of AWGs is their flexibility about the possibility to insert several input waveguides since they are not on the same side than the output waveguides. Indeed, hitting the target wavelength might be a difficult task and there is usually a shift between simulations and measurements. Therefore, if the light is sent through another input waveguide along the Rowland circle [57] of the first FPR, the device's spectra can be shifted. Finally, AWGs are dominant in dense wavelength-division multiplexing (DWDM) due to the high number of channels required, their flexibility and footprint and low fabrication constraints. Typical AWGs can support 32 channels spaced at 100 GHz apart (0.8 nm) within the C-band spectrum (1550 nm) [58]. Large scale 25-GHz-spacing 400-channel AWGs have also been developed [59]. However, as the device's footprint increases with the number of channels, other technologies were developed. An AWG with overlapping FPRs was demonstrated in [60]. It is also possible to flatten the device's frequency response by inserting a multi-mode interferometer at the input waveguide, but then at the cost of higher insertion losses [20, 61]. The AWG is one of our selected technology for wavelength division multiplexing.

3.3.2 Reflective arrayed waveguide gratings

One way to reduce the AWG footprint consists in removing one FPR and using a reflective structure in the arrayed waveguide section. The AWG's footprint is then reduced by a factor of 2. As opposed to conventional AWGs, a RAWG has the input waveguide on the same side as the output waveguides. The arrayed waveguides start from the FPR and are ended with either conventional mirrors or with photonic crystal reflectors. However, dielectric or metal films are required for conventional mirrors and the cleaved facets need to be critically smoothed [60, 62] and photonic crystal structures also make the fabrication more challenging [63].

3.3.3 Echelle diffraction gratings (EDGs)

An EDG consists of an FPR with a reflection grating on one side and, on the other side one input and several output waveguides. This device provides low insertion loss and good crosstalk levels (below -20 dB) [60]. The phase delay is provided by the facets of the device. Moreover, the insertion loss can be further improved by adding Bragg mirrors at the facets [60]. The EDG's footprint can be smaller than the AWG's in CWDM. However, in DWDM the AWG can be smaller than the EDG [64]. In addition, this type of device requires smooth and deeply etched grating facets to limit excess loss [60, 65] and the input waveguide is situated on the same side of the output waveguides, limiting its flexibility compared to the AWG.

3.3.4 Cascaded Mach-Zehnder interferometers

Cascaded MZIs are another type of demultiplexing devices and consist of cascaded filters which are composed of two power splitters connected by an upper and lower arm, with a path length difference. The power splitters are either directional couplers (DC) or multi-mode interferometers (MMIs). MZI filters have the advantage of being easy to design and to manufacture, which make them a good alternative to AWGs in CWDM. However in DWDM, when the number of channels exceeds 4, the MZI becomes larger than the AWG. In addition, this type of device provides low insertion loss [66,67] and low crosstalk level can be achieved with either stage doubling [67, 68] or with MMIs as shown in Paper [A]. Thus, this device was selected in addition to the AWG for comparison.

3.3.5 Cascaded multimode waveguide gratings

Cascaded multimode waveguide gratings (MWG) are basically contra-directional grating coupler-based devices. The major advantage of grating-based devices is the reduced footprint [67]. The input light source is directed to a multimode waveguide section and into a grating where the desired wavelength is coupled back into an output single mode waveguide. Previous works demonstrated four-channel CWDM cascaded MWG in the O-band (1240-1360 nm) with channel spacing of 20 nm, insertion loss below 1 dB and crosstalk level below -20 dB [69]. However, this kind of technology requires strong grating apodization to achieve low level crosstalk and strong corrugation depth to obtain flat-top channel response [69, 70].

3.3.6 Microring resonators

Microring resonators (MRR) are similar to MWGs and could constitute a nice alternative to AWGs. Indeed AWGs can suffer from random phase errors due to deviation from fabrication [71] and MRRs have the potential of being compact, and in addition having low loss. However, multi-microrings are necessary to achieve flat-top response and low crosstalk level [72], thus increasing the sensitivity to fabrication inaccuracies [73].

3.4 Power splitters

This section focuses on two kinds of power splitters used in cascaded MZIs, namely the MMI and the directional coupler.

3.4.1 Multimode interferometers (MMIs)

The structure of a MMI consists of a group of input/output single mode waveguides and a wide multimode waveguide in the middle. This type of device has the advantage of being broadband and tolerant to fabrication deviations [74]. The input field comes from one of the two input waveguides and propagates through the multimode section. Imaging of the input field can be achieved when the length of the device is set as shown in Figure 3.4 [75]:

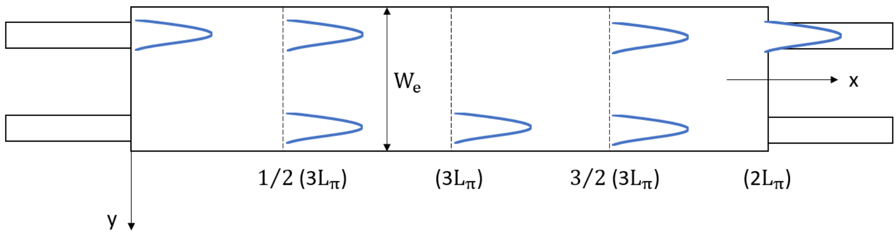

Figure 3.4: Field pattern (represented in blue) in a 2 x 2 MMI when the light comes from the upper input waveguide.

L_π is the beat length of the two lowest order modes in the MMI section and is given by [61]:

$$L_\pi = \frac{4 n_r W_e^2}{3\lambda_0}, \tag{3.3}$$

where n_r is the refractive index of the waveguide, W_e the effective width of the MMI and λ_0 the wavelength. When the length L of the multimode section is set as $L = 3/2\ L_\pi$, double imaging of the input field is realized with a loss of 3 dB for both output fields [75]. This is the length we want to select for our device to obtain a 3 dB coupler. A scheme of the designed MMI in Paper [A] is presented in Figure 3.5.

The example manufactured and discussed in Paper [B] is a 2 x 2 MMI (two input and two output waveguides) and consists of a $W = 8$ μm wide and $L = 70$ μm long slab-waveguide. The input and output waveguides are spaced by $W/3$ and are linearly tapered to reduce the

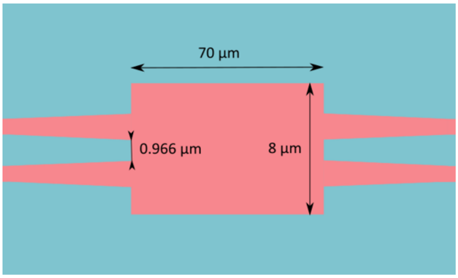

Figure 3.5: Illustration of the designed 2 x 2 MMI.

insertion loss introduced by the device [67]. However, these devices are more difficult to design for arbitrary cross coupling coefficients [67]. The device was designed with mode-solution Lumerical software, using both EME and varFDTD solvers. The results of the simulations are shown in Figure 3.6.

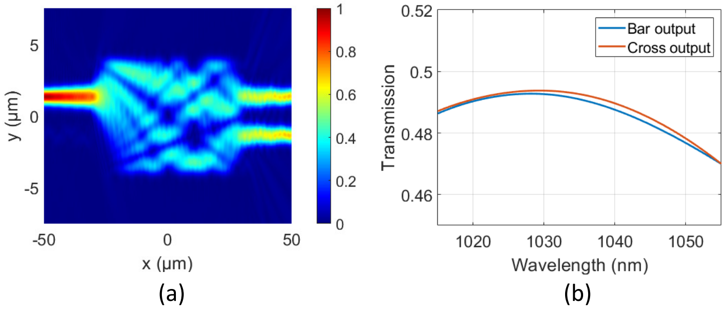

Figure 3.6: (a) varFDTD simulated power distribution of the MMI for the TE mode. (b) Transmission of the MMI. The 'Bar' and 'Cross' outputs are respectively the upper and lower outputs when the upper input is selected.

3.4.2 Straight directional couplers (DCs)

The DC can be described as a set of two parallel waveguides enabling the transfer of light from one waveguide to the other through evanescent coupling. The device is characterized by 4 ports (2 inputs and 2 outputs) and a straight section in which the light coupling occurs. DCs are attractive due to their low insertion loss, compactness and are easy to design for arbitrary cross coupling coefficients. The main characteristics that determine the cross coupling coefficient are the waveguide dimensions, the gap between the waveguides in the straight section and the length of the latter. However, straight DCs are more wavelength dependent than MMIs [67] and less tolerant to fabrication deviations. In Paper [A], three DCs were designed for following cross coupling coefficient: K = 0.5, 0.29 and 0.08 [20, 66]. The length L of the straight section and the gap g between the waveguides were chosen as L = 20 μm and g = 300 nm for K = 0.5, L = 13 μm and g = 300 nm for K = 0.29, L = 13 μm and g = 440 nm for K = 0.08. The field profiles and the transmissions of the DCs are shown in Figures 3.7 and 3.8.

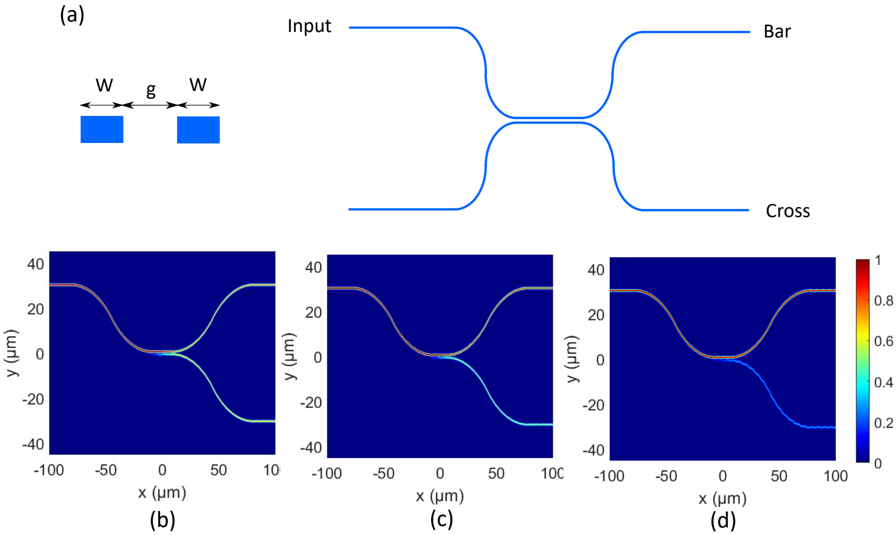

Figure 3.7: (a) Drawing of a straight conventional DC with cross section of the coupling region. VarFDTD simulated power distribution of the DC for K = (b) 0.5 (c) 0.29 (d) 0.08 for the TE mode.

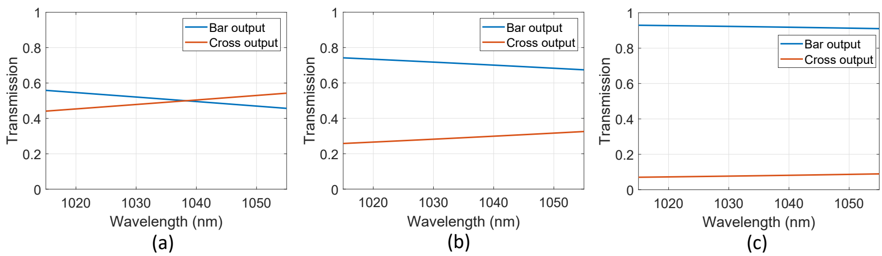

Figure 3.8: Transmission of the DC for K = (a) 0.5 (b) 0.29 (c) 0.08.

3.4.3 Curved DCs

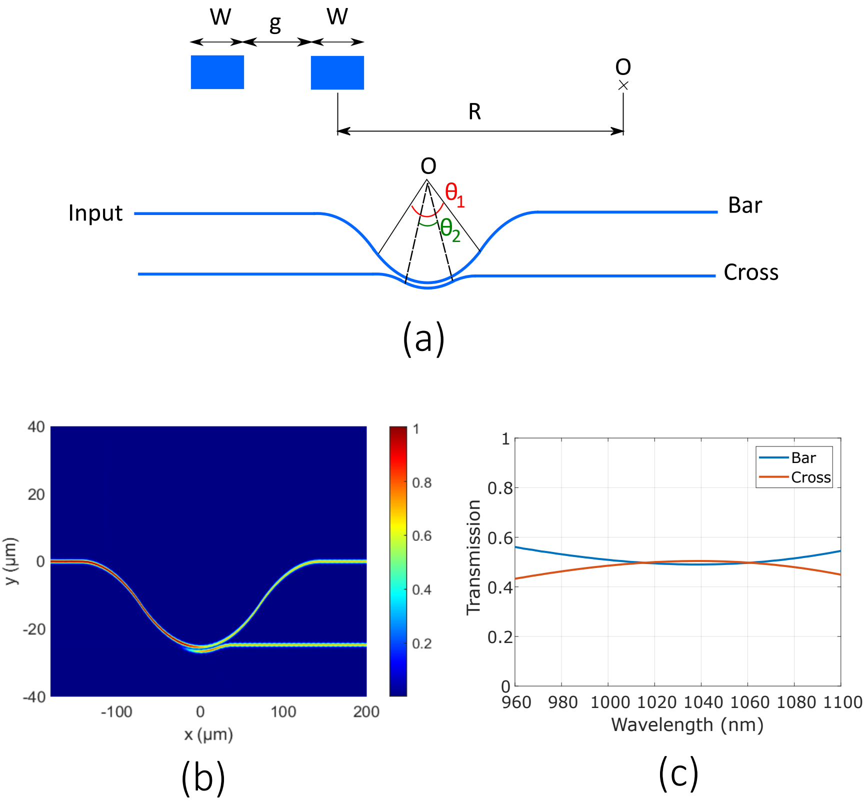

Figure 3.9: (a) Cross section of the curved DC with a scheme of the full device. Here, g = 340 nm, R = 210 μm, θ_1 = 40° and θ_2 = 10.82°. (b) Electric field profile of the curved DC. (c) varFDTD simulation of the transmission of the device for the 50:50 splitting ratio.

The main disadvantage of straight DCs is the wavelength dependence of their transmission due to the the fact that the effective index n_{eff} of the mode propagating through the waveguide depends on the wavelength. This causes increased crosstalk in demultiplexers based on cascaded MZIs [20, 67]. Therefore, one technique to compensate for the wavelength dependence of n_{eff} consists in curving the coupling region of the DC as shown in Figure 3.9. This device requires careful optimizations of the radius R of the curved section, the gap g, and the angle θ. A broadband

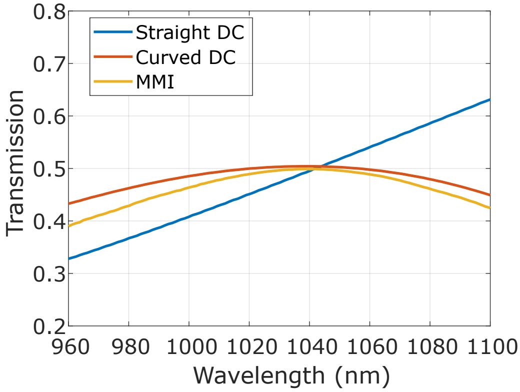

Figure 3.10: Comparison of the simulated (with varFDTD) cross output transmission of the straight, curved DC and MMI for the 50:50 splitting ratio.

silicon on insulator DC combining curved with straight sections has also been demonstrated [76].

In Figure 3.10 is plotted the simulated transmission of the straight/curved DCs and MMI. It can be observed that the curved DC has a larger bandwidth than the MMI. However, the smaller bandwidth of the MMI is compensated by its good tolerance to manufacturing deviations. As no curved DCs have been manufactured during this thesis, we have no characterization results for these components.

3.4.4 Fabrication and measurements of power splitters

Figure 3.11 shows simulation and characterization results of the straight DC and the MMI for the 50:50 splitting ratio. The measurements are taken by cascading 4 devices for the MMI and 3 devices for the DC (one DC presented an additional loss of 4 dB and was possibly damaged). The measurements in overall are in good agreement with the simulations. The measured average splitting ratio for the DC is 55:45 and the MMI has a measured transmission of 0.47 at 1035 nm, which represents an output power of 3.4 dB for both output waveguides. Therefore, the MMI has a measured average additional loss of 0.4 dB. One can notice the strong oscillations on the measured transmission of the DC, which are smaller for the MMI.

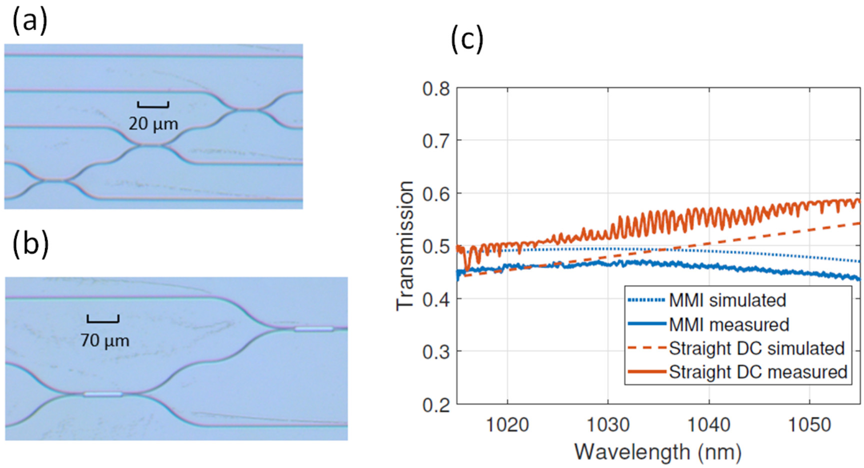

Figure 3.11: Microscope image of (a) cascaded straight DCs and (b) cascaded MMIs). (c) Simulation (dashed curves) and measurements (continuous curves) of straight DCs and MMIs.

3.5 Design of CWDM demultiplexers

This section focuses on design and measurements of AWGs and cascaded MZIs at 1 μm. It is also an extension of Paper [A] which does not include all measurements of the cascaded MZIs.

3.5.1 Design of AWGs

The AWG design in this thesis is conventional. For both FPRs of the device, the input and arrayed waveguides are separated by a distance of respectively $\mathrm{d_r}$ and $\mathrm{d_a}$ along the FPR as illustrated in Figure 3.12. As explained in section 3.1, the different parameters set the FSR and the wavelength channel spacing.

With the input and output star couplers of the AWG being identical, following conditions should be satisfied [77]:

$$\lambda_0 = \frac{\mathrm{n_c}\Delta\mathrm{L}}{\mathrm{m}}, \tag{3.4}$$

where m is the diffraction order of the AWG, $\Delta\mathrm{L}$ the length increment between the array waveguides, $\mathrm{n_c}$ the effective index of the arrayed waveguides, λ_0 the central wavelength. The the free spectral range (FSR) in the frequency domain is related to the diffraction order m of the AWG

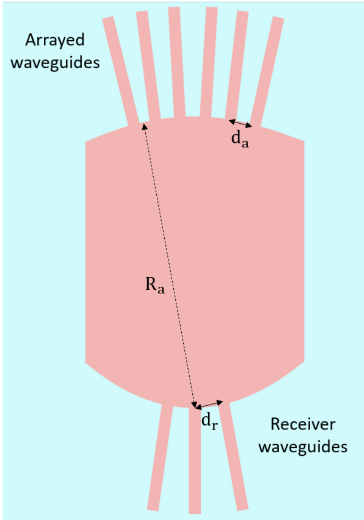

Figure 3.12: Scheme of the AWG star coupler

with following equation [36]:

$$\mathrm{FSR}_{\nu} = \frac{\nu_0}{\mathrm{m}}, \tag{3.5}$$

where ν_0 is the center frequency. To maintain a low loss non-uniformity for the outer channels, the FSR in the wavelength domain should at least be equal to $\mathrm{N}\times\Delta\lambda$ [34], where N is the number of channels and $\Delta\lambda$ the channel spacing. Then with the combination of equations 3.4 and 3.5, we can deduce the length increment as a function of the FSR in the frequency domain:

$$\Delta\mathrm{L} = \frac{\mathrm{c}}{\mathrm{n_c}\mathrm{FSR}_{\nu}}, \tag{3.6}$$

where c is the vacuum speed of light. The central wavelength, wavelength channel spacing and the FSR are set before designing the device.

Measurements and a more thorough analysis about this component are provided in Paper [A]. In addition, measurements of AWGs for DWDM applications are shown in Chapter 6 of the thesis.

3.5.2 Design of cascaded MZIs

The cascaded MZI consists of three filters cascaded in two stages as shown in Figure 3.13 when the device has 4 channels. The first stage separates the odd from the even wavelengths and also determines if the MZI response will be either Gaussian or flat-top. A first order filter in Stage 1 leads to a Gaussian response and a second order filter leads to a flat-top response. For a Gaussian MZI filter, only power splitters with a cross coupling coefficient K = 0.5 is necessary. However, to obtain a flat-top response, cross coupling coefficients of K = 0.5, 0.29 and 0.08 (for a second order filter) have been suggested [20, 66]. The two MZI orders are presented in Figure 3.14.

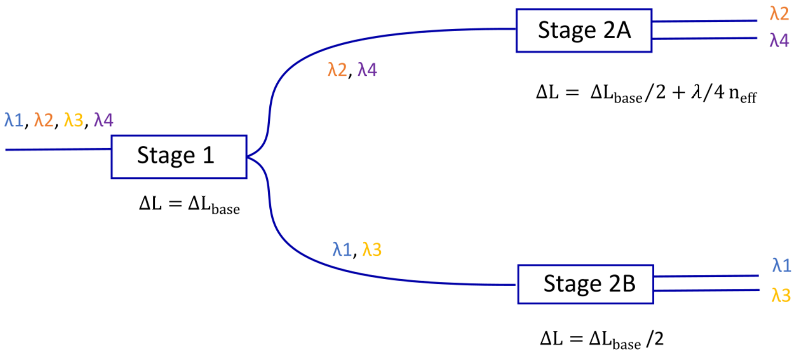

Figure 3.13: Diagram of a cascaded MZI. λ is noted as the center wavelength.

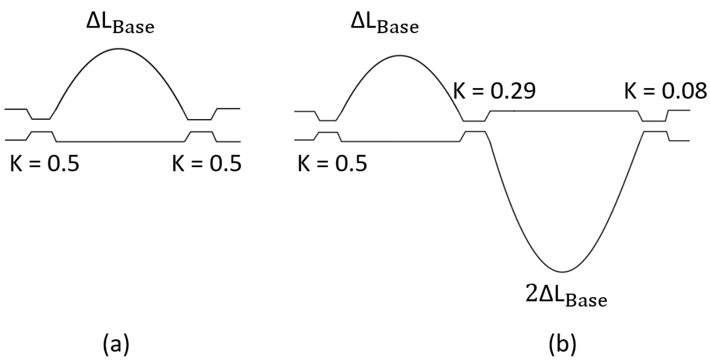

Figure 3.14: Schemes of first order (a) and second order (b) MZI filters. The K coefficients refer to the cross coupling coefficients of the directional couplers (or MMIs).

The free spectral range (FSR) is determined by the central wavelength λ, the waveguide group index n_{gr} and the base length difference ΔL as [78]:

$$\mathrm{FSR}_{\lambda} = \frac{\lambda^2}{\mathrm{n_{gr}}\Delta \mathrm{L}}. \tag{3.7}$$

The base length difference for the first stage of the cascaded MZI can be deduced by [78] ($\delta\lambda$ being the channel spacing):

$$\Delta \mathrm{L_{Base}} = \frac{\lambda^2}{2\delta\lambda \mathrm{n_{gr}}}. \tag{3.8}$$

Each stage is then simulated separately. The first has a FSR of 16 nm and the second a FSR of 32 nm. The calculated base length difference is around 35.76 μm for the first stage and 17.88 μm for the second (an additional shift is necessary for the stage 2A in Fig. 3.13). Fig. 3.15 shows the simulations for each stage when the used power splitters are directional couplers (DCs).

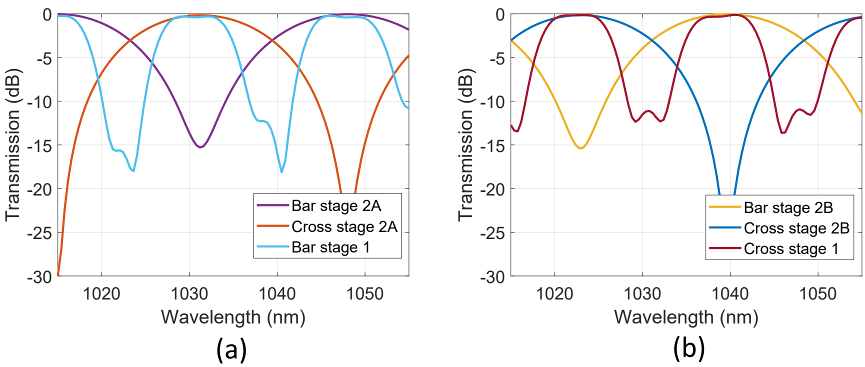

Figure 3.15: Simulation of (a) the upper arm MZI filter (Stage 2A) and (b) the lower arm MZI filter (Stage 2B)

The simulations reveal the high crosstlalk level (around -12 dB) of the flat-top MZI in the first stage when using straight directional couplers for all cross coupling coefficients. This is due to the high wavelength sensitivity of the straight directional couplers [67] as reported earlier. The use of broadband bent-directional couplers [20,67] or MMIs [67] can significantly reduce the crosstalk level.

3.5.3 Fabrication and measurements of cascaded MZIs

We manufactured cascaded MZIs based on DCs only and cascaded MZIs based on both MMIs and DCs as shown in Figure 3.16. In Figure 3.16a are shown two devices based on DCs only. For the device in Figure 3.16b, we used 50:50 MMIs instead of 50:50 DCs. For the other splitting ratios however (71:29 and 92:8), MMIs were more difficult to design without additional losses. Therefore, we kept straight DCs for these splitting ratios. The characterization and simulation results of the three devices are shown in Figure 3.17. The cascaded MZI based on DCs and MMIs in Figure 3.16 is the one presented in Paper [A] and the simulated 1×8 and 1×16 flat-top DEMUX are also based on this design.

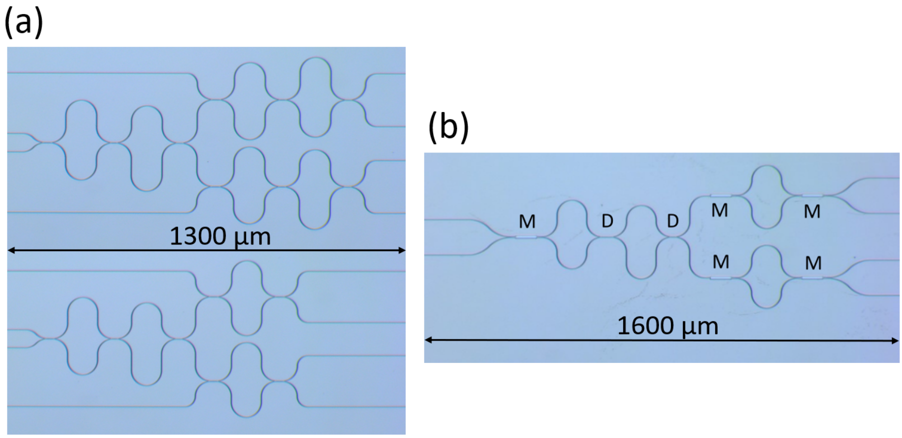

Figure 3.16: (a) Manufactured cascaded MZIs based on DCs exclusively. The bottom device is a 2nd-to-1st order filter and the top device is a 2nd-to-2nd order filter. (b) Manufactured cascaded MZIs based on DCs and MMIs. The 'M' and 'D' letters and for MMI and DC respectively.

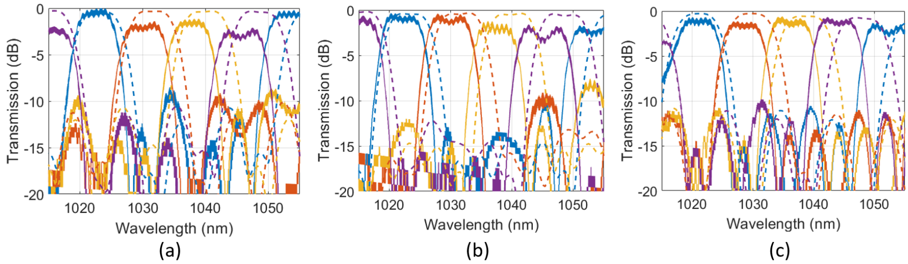

Figure 3.17: Simulation (dashed curves) and measurements (continuous curves) of the (a) 2nd-to-1st order MZI filter based on DCs, (b) 2nd-to-2nd order MZI filter based on DCs, (c) cascaded MZI based on DCs and MMIs.

3.6 Conclusions

In this chapter we proposed an integrated solution for WDM optical interconnects at 1060 nm and focused on demultiplexers. In Paper [A], we extrapolate with simulations the comparison between AWGs and cascaded MZIs for 8, and 16 channels. Gaussian and flat-top devices were compared for each case. The characterizations showed that the cascaded MZIs had better tolerance to manufacturing deviations and proved to be promising for CWDM. However, as explained in Paper [A] at 16 channels, there is a tradeoff between size and writing field.

CHAPTER 4

Grating couplers

One of the main challenges of silicon photonics is to couple the light from an optical fiber into an integrated on-chip-waveguide while maximizing the optical bandwidth and minimizing the loss. One possibility is to directly couple the light into the input waveguide in the chip-plane with the help of inverse tapers [8] but this generally requires lensed fiber or high numerical apertures to focus the optical beam into the waveguide. Another technology consists in using 3D-taper structures but such tapers require gray scale lithography which is difficult to control and thus potentially lead to fabrication deviation [79, 80]. However, another possibility consists in coupling the light from above the chip with the help of grating structures which collect the fiber mode and couple it into the waveguide. Such structures are either straight or focusing and are approximately 10 to 18 μm wide depending on the size of the fiber mode on top of the chip. Grating couplers are of interest because of their compact size and not requiring polishing facets for coupling [80]. This chapter explores the theoretical aspect of grating couplers, the optimization methods for enhancing the coupling efficiency and compares straight gratings with focusing gratings.

4.1 Theory

The diffraction behavior of a grating coupler is described by the Bragg condition, expressed as [81]:

$$\mathbf{k_0}\mathrm{sin}\Phi + \mathrm{m}\mathbf{G} = \boldsymbol{\beta}_\mathrm{m}, \tag{4.1}$$

where $\mathbf{k_0}$ is the wavevector of the incident beam, Φ the angle of incidence, m the diffraction order, $\mathbf{G}$ the grating vector and $\boldsymbol{\beta}_\mathrm{m}$ the propagation constant of the coupled beam into the grating. Then, the grating period Λ can be deduced as [82]:

$$\Lambda = \frac{\lambda}{\mathrm{n_{eff}} - \mathrm{sin}\Phi}, \tag{4.2}$$

where $\mathrm{n_{eff}}$ represents the effective index of the grating and λ is the free space wavelength. To avoid strong second order diffraction into the cladding layers and thus loss increment, the fiber is always tilted [82]. With f being the filling ratio of the grating, the grating effective index of the fundamental propagating mode can be expressed as:

$$\mathrm{n_{eff}} = \mathrm{fn_{etch,\,eff}} + (1 - \mathrm{f})\mathrm{n_{slab,\,eff}}, \tag{4.3}$$

The coupling loss of the device is composed with the back reflection of the beam at the top cladding/air interface, the absorption into the Si substrate, the diffracted power into the cladding and the transmitted power. The transmitted power through the waveguide then can be expressed as following [81]:

$$\mathrm{P_{transmitted}} = \mathrm{P_{incident}} - \mathrm{P_{substrate}} - \mathrm{P_{reflection}} - \mathrm{P_{out}}, \tag{4.4}$$

where $\mathrm{P_{incident}}$ is the amount of incident power coming from the fiber, $\mathrm{P_{substrate}}$ the amount of power lost into the Si substrate, $\mathrm{P_{reflection}}$ the power reflected on the grating coupler and $\mathrm{P_{out}}$ the power coupled into the opposite waveguide. Figure 4.1 presents the different losses of a grating coupler.

A large amount of the incident power is reflected on the grating coupler into the air, which limits the coupling efficiency. However, with a top SiO_2 cladding layer, the refractive index contrast is reduced and the phase matching condition changes [83]. Therefore, this will cause a reduction of the reflection into the air and increases the coupling efficiency [84] as indicated in Figure 4.2.

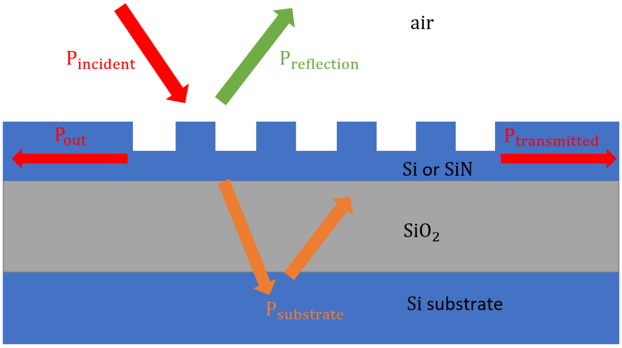

Figure 4.1: Illustration of a grating coupler

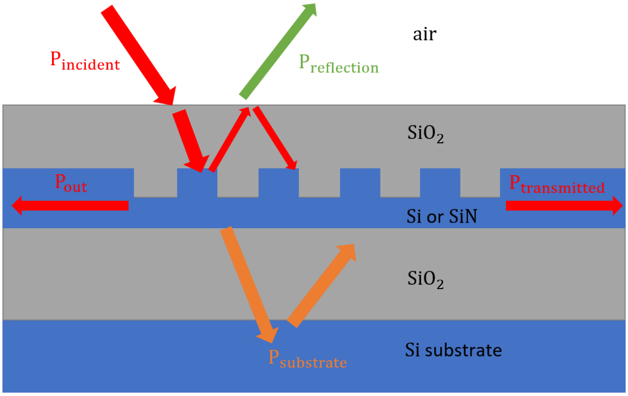

Figure 4.2: Illustration of a grating coupler with a top cladding

4.2 Techniques to improve the coupling efficiency

4.2.1 Apodization

The issue of a uniform grating is that the coupled beam has an exponential decaying power instead of being Gaussian [82, 85]. To reduce the coupling loss, the apodization technique can be used. It consists in modulating the fill factor or the periodicity along the propagation direction [82] as shown in Figure 4.7. Then, an even further step based on inverse design could be applied to enhance the coupling efficiency and the bandwidth [86].

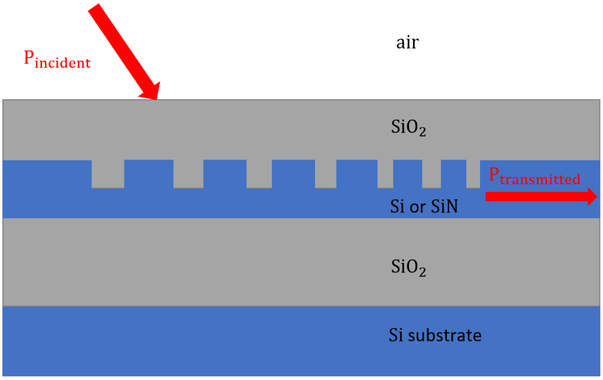

Figure 4.3: Illustration of an appodized grating coupler

4.2.2 Bottom distributed Bragg reflector

A multilayer distributed Bragg reflector (DBR) placed between the substrate and the buried oxide cladding (BOX) can significantly improve the coupling efficiency. A DBR is a stack of multilayer film with alternate material layers such as SiO_2 and SiN. Such a multilayer stack can be deposited with a sputtering method, LPCVD or using Liquid Source Chemical Vapor Deposition (LSCVD) [87]. A grating coupler based on a SiN waveguide with $N = 20$ layer SiO_2/SiN DBR with a coupling efficiency of -1.75 dB has been demonstrated [87]. For comparison, a grating coupler without a bottom reflector was manufactured and the measured coupling efficiency was -5 dB [87]. To provide such a coupling efficiency, a DBR reflectivity close to 100 % is needed.

4.2.3 Growth overlay

Another method consists in adding a poly-silicon overlay layer on top of the grating prior to the etching. The selected material for the overlay has to induce the required phase change [82]. The advantage of an overlay layer is that it can prevent the need of adding a bottom DBR reflector as demonstrated in [88] with a silicon overlay layer. Indeed, a silicon overlay increases the directionality of the device by creating constructive interference towards the fiber and destructive interference downwards to the silicon substrate [81].

4.2.4 Staircase design

A two-step staircase design also improves the directionality by creating a blazing effect [89, 90]. This innovation consists of a two-step etching of the grating layer and the fiber is placed in the contra-directional coupling configuration as described in [89]. A two-step staircase design is also used in Paper [B]. In Figure 4.4 is shown the difference in coupling efficiency and bandwidth between a conventional and a staircase grating coupler.

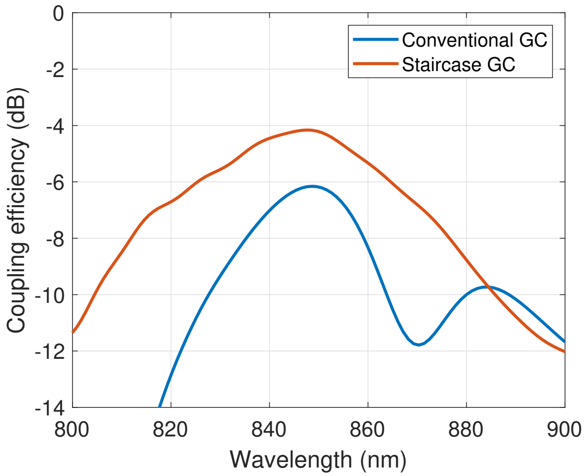

Figure 4.4: 2D FDTD Simulations of coupling efficiency of a conventional GC and a staircase GC for D = 145 μm and $\Phi = 11°$ for the contra-directional case. The grating period are respectively 465 nm and 480 nm for the conventional and the staircase GC.

4.3 Grating couplers for VCSEL arrays at 1 μm

To meet the requirements specified in chapter 3, the grating couplers for all four channels are manufactured in the same chip with a bottom DBR between the Si substrate and the bottom cladding. The material used for the grating coupler is SiN and the waveguide is 160 nm thick. The grating is fully etched as shown in Figure 4.5. All the simulations for the grating

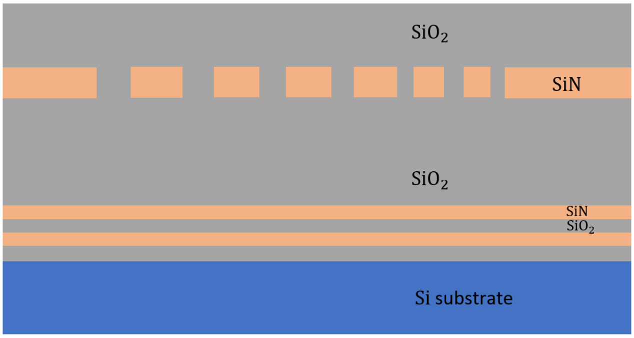

Figure 4.5: Schematic illustration of the apodized DBR-based grating coupler. The real device has 20 grating lines and 6 pairs of SiO_2/SiN bottom layers.

optimizations are carried out in 2D-FDTD. The initial grating period for each channel is different to meet the Bragg condition in equation 4.2 and each device has 20 grating lines. For the DBR, two material options were available: a DBR based on SiO_2 and SiN, or one based on SiO_2 and TiO_2. The TiO_2 material had the advantage over SiN of providing a large bandwidth but one fabrication step included an annealing process, which the TiO_2 material did not survive. Therefore, SiN was finally selected as the second material for the bottom DBR. Figure 4.6 shows the reflectivity of a manufactured 6 pair SiO_2/SiN DBR. The thickness of the SiN and SiO_2 layers of the bottom DBR are respectively 129.117 nm and 178.63 nm.

To optimize the coupling efficiency, a critical control of the top and bottom cladding thicknesses is needed. The top cladding is 2760 nm thick and the bottom cladding is 1850 nm thick. The final step of the coupling efficiency optimization is to apodize the gratings. The length as well the position of each grating line are swept. The final result of the optimized coupling efficiencies of the four channels is presented in Figure 4.7. Channel No. 1 which is optimized for a target wavelength of

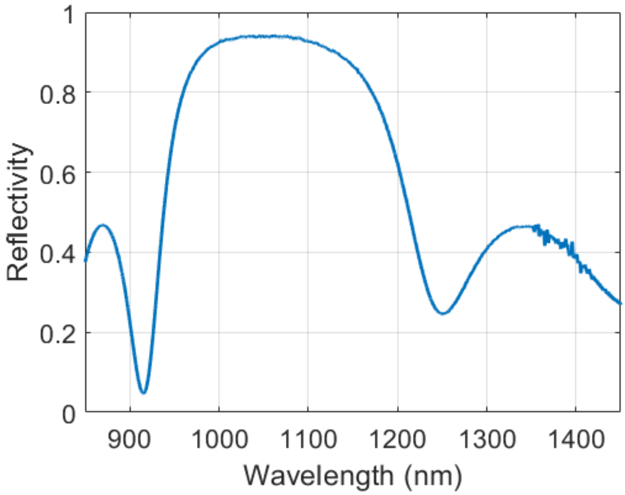

Figure 4.6: Measured reflectivity of a 6 pair SiO_2/SiN DBR. The measured peak reflectivity is 0.94.

1023 nm presents the lowest coupling efficiency (-1.5 dB) while having the largest bandwidth. The highest efficiency obtained is -1 dB with channel No. 3. at 1039 nm.

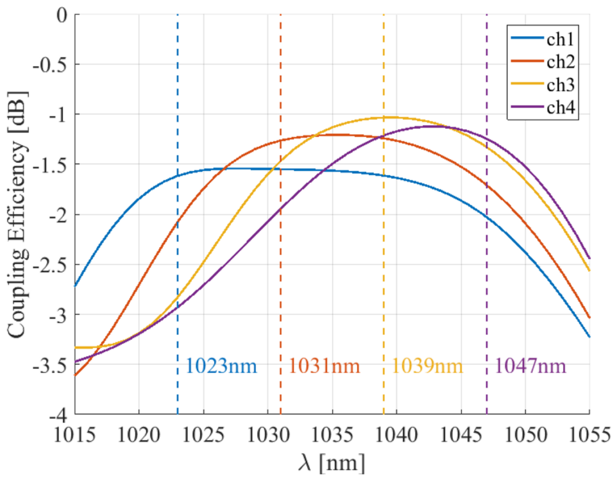

Figure 4.7: 2D-FDTD Simulations of coupling efficiency of the channel array.

4.4 Types of grating couplers

In this thesis, 1D-structural grating couplers are investigated. The first and simplest design is the straight grating coupler, which consists of linearly enlarging the grating lines in the direction perpendicular to the propagation of the light. The grating lines should be wide enough to collect most of the light coming from the fiber (10 to 18 μm wide). Thus, an adiabatic taper is necessary to convert the light from the slab into the single-mode waveguide. Another design is the focusing grating coupler which consists of elliptically curving the grating lines to avoid the use of a long-taper and thus to reduce the device's footprint.

4.4.1 Straight gratings

Typical straight grating couplers have a grating section that is between 15 and 30 μm long and 10 to 18 μm wide to collect 100 % of the incoming beam from the fiber/VCSEL. The light is then coupled into a slab-waveguide that is as wide as the grating and finally converted into the single-mode waveguide with either a linear or an adiabatic taper. To achieve a good conversion efficiency, the taper needs to fulfill the adiabatic condition which requires a minimal taper length depending on the width of the slab section [91]. In Figure 4.8 we show the conversion efficiency of the linear taper converting the mode from the 12 μm wide slab-waveguide to the 0.9 μm wide single mode waveguide. From the simulation, a taper length of 100 μm should already ensure a conversion efficiency of -0.3 dB. The electric field profile of a straight grating coupler with a 100 μm-long taper is presented in Figure 4.9. We can clearly observe an adiabatic conversion of the fundamental optical mode coming from the slab-waveguide into the fundamental mode of the single-mode waveguide. To avoid additional losses coming from the fabrication, a taper length of 400 μm was selected.

An example of a straight grating coupler is also proposed in Paper [B] in which the grating section is 10 μm wide and between 17 and 21 μm long. The taper of the device is 300 μm long. Such grating couplers are efficient but have a large footprint due to their ultra-long conversion tapers. However, ultra-short tapers with conversion efficiencies of 96 % have been demonstrated at 1550 nm on Si-waveguides [92].

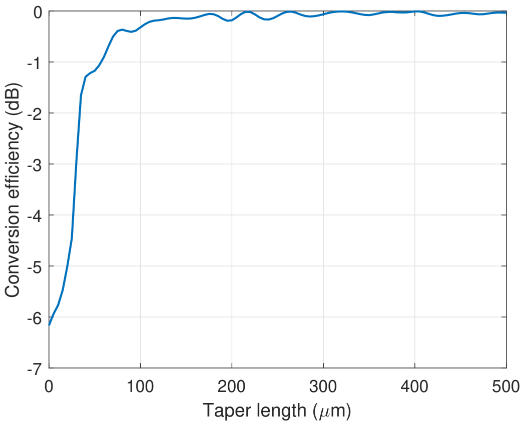

Figure 4.8: EME Simulation of the conversion efficiency of a linear taper. The slab-waveguide is 12 μm wide and the output waveguide 0.9 μm wide for a thickness of 160 nm.

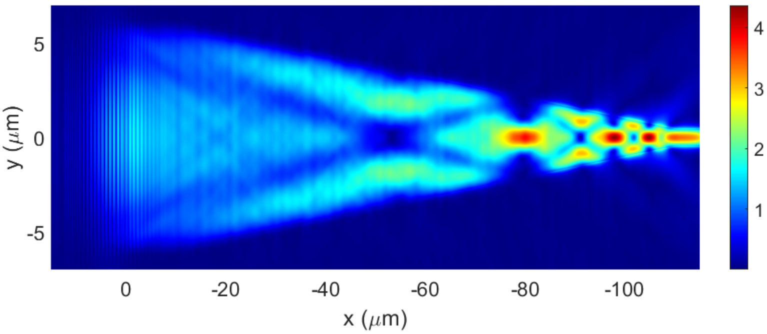

Figure 4.9: Electric field profile of a straight grating coupler with a 100 μm-long linear taper

4.4.2 Focusing gratings

Another way to reduce the size of the grating coupler while keeping a decent coupling efficiency consists in curving the grating lines so that the incoming beam is focused into the taper. The curvature is calculated with following equation [81, 93]:

$$q\lambda = \mathrm{x n_{cladding}} \cos\theta - \mathrm{n_{eff}} \sqrt{\mathrm{y^2 + x^2}}, \tag{4.5}$$

where q is the grating line number, x the coordinate of the propagation direction and y the coordinate in the lateral direction, n_{eff} the effective index of the coupled mode, $n_{cladding}$ the refractive index of the top cladding (or air if there is no cladding) and θ the coupling angle. The device (taper included) will have a length of approximately 40 μm which is 10 times smaller than a conventional straight grating coupler here. Figure 4.10 shows a drawing of a focusing grating coupler.

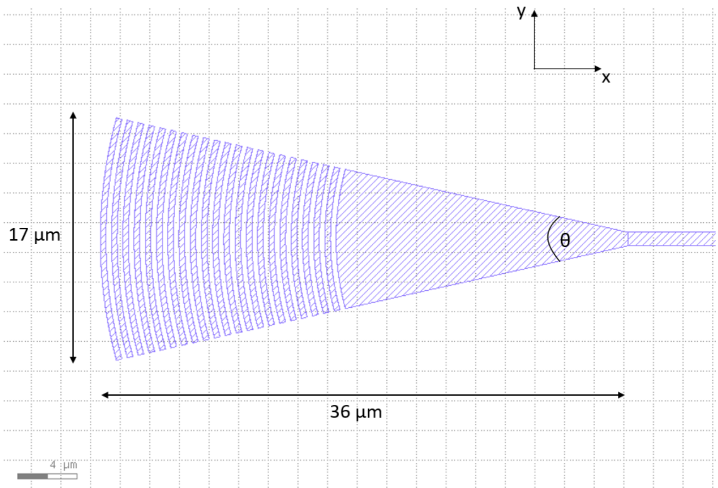

Figure 4.10: Designed focusing grating coupler in KLayout.

The positions of the grating lines of the apodized grating couplers simulated in 2D-FDTD are then implemented into the focusing designs in 3D-FDTD. In Figure 4.11 is the simulation result of the apodized focusing grating coupler corresponding to channel No. 3 (1039 nm).

The coupling efficiency at 1039 nm reached -1.5 dB, which is still within the target efficiency (power budget for the grating couplers: -2 dB). The device also has a 3 dB-bandwidth of 39 nm.

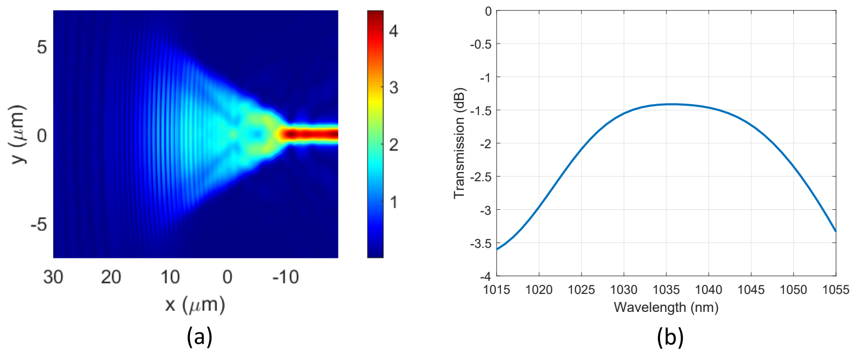

Figure 4.11: 3D-FDTD simulation an apodized focusing grating coupler (channel 3: 1039 nm) with a bottom DBR. (a) Electric field profile of the grating in the xy plan. (b) Coupling efficiency of the device.

4.4.3 Fabrication and comparison of the devices

Straight and focusing grating couplers were manufactured to compare their real performance. To measure the gratings coupling efficiencies, the test circuit is constructed with two identical grating devices connected with a single-mode waveguide as shown in Figure 4.12. In the characterization stage, the SMFs are tilted by an angle of 8°. In this fabrication run however, the bottom SiN/SiO_2 is not included and the BOX and cladding thicknesses are not optimized. Indeed, the thickness of the top and bottom SiO_2 cladding is 3 μm. In addition the measured thickness of the SiN layer is 175 nm. Figure 6.5 shows the manufactured devices for characterization. Among them are focusing devices and three straight devices, each corresponding to one specific wavelength channel (see Figure 4.7). The gratings were also apodized to improve the coupling efficiency.

Figure 4.12: Scheme of the characterization of the grating couplers showing the tilted input/output cleaved SMFs

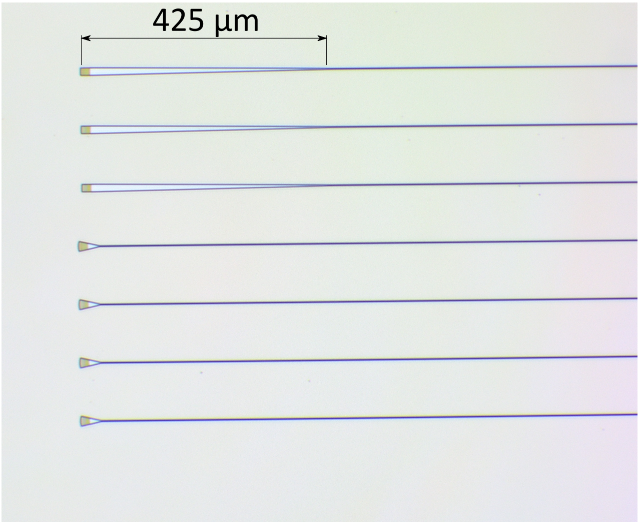

Figure 4.13: Manufactured apodized straight and focusing grating couplers

Figure 4.14 presents for channels No. 2 and 3 the measurement of the coupling efficiencies of the straight and focusing grating couplers. 2D-FDTD simulations are added for comparison. It can be observed that the focusing grating coupler has a slightly better coupling efficiency than the straight one in both case, in addition to have a much smaller footprint. The expected coupling efficiency from simulations was circa -4.9 dB and the measured coupling efficiency per device is -7.7 dB. The 2.8 dB difference between the simulations and the measurements could be due to possibly improper fiber-device alignment. For the GC-measurements, cleaved lensed fibers were used, so improper cleaving of the fibers could also decrease the quality of the characterization. Measurements with lensed fibers were also realized for comparison and the coupling efficiency

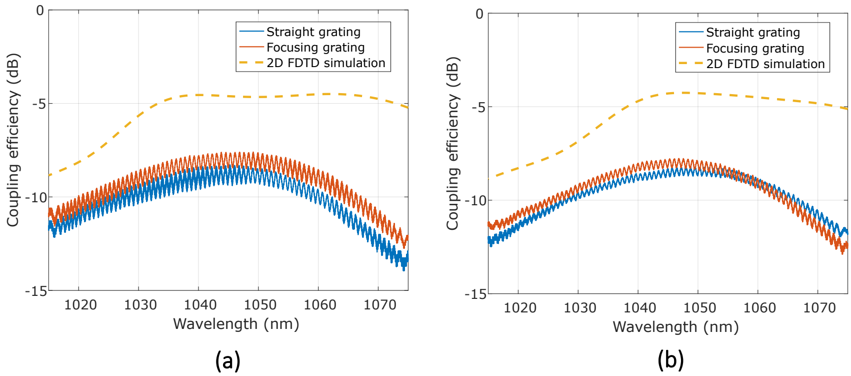

Figure 4.14: Measured coupling efficiencies of the apodized straight and focusing grating couplers for (a) channel No. 2 and (b) channel No. 3. 2D FDTD simulation of the corresponding grating coupler is also included.

was reduced down to -13 dB as the spot size is 2.5 μm instead of 6 μm. Improper etching of the SiN layer or deviation in the thicknesses of the different layers (cladding, SiN) could also be sources of discrepancy.

CHAPTER 5

Receiver platform for CWDM at 1 μm

This chapter focuses on the integrated receiver side of the optical interconnects and review the platform considerations treated in Papers [C] and [D]. The critical issue of the receiver is dealing with the polarization of the light at the output of the single-mode fiber, which is randomly changing. Indeed, in contrast to polarization maintaining fibers, conventional single mode fibers do not maintain the initial polarization of the light at the input through propagation. The first problem of polarization maintaining fibers is their high cost due to their manufacturing complexity. The other issue of polarization maintaining fibers is their high propagation loss with respect to standard single-mode fibers. Therefore, only conventional single mode fibers are considered for low cost optical interconnects, which is why the receiver must work without depending on the polarization state of the light coming from the fiber. In this chapter, we will go through the platform considerations and the main simulation results.

5.1 Platform considerations

To build a polarization independent WDM receiver, one possibility is based on a two-dimensional polarization independent grating couplers [81]. Small footprint structures have also been demonstrated on SOI platform in Ref [94]. However, despite the relaxing tolerance to fiber misalignment this device offers, the big remaining drawback is the significant coupling loss, which is between 7 and 11 dB. A bottom reflector [87, 95] between the substrate and the buried oxide layer would increase the coupling efficiency of the device. Other possibilities consist in manufacturing reflectors at the back of the grating, such as corner mirrors [96] or using sub-wavelength blazed structure [97]. The blazed structure experimentally demonstrated on SOI in Ref [97] a coupling loss within 5 dB with a polarization dependent loss around 1.5 dB. However, to reduce the coupling loss and the manufacturing complexity of the receiver, we considered first the edge coupling solution instead of the surface coupling one.

The first and simplest solution to design a polarization independent receiver consists in the use of a square single mode waveguide, ensuring identical effective index whether the incoming beam has a TE or TM polarization. The advantage of a square waveguide is the reduced footprint of the receiver due to the reduction of unnecessary components (polarization splitters, rotators) and the reduced size of the demultiplexers due to stronger mode confinement in the waveguide. However, the cons of thick square single-mode waveguides is the increased propagation loss of due to roughness on the sidewalls [98]. In addition, improper etching of the waveguide can also reduce the polarization tolerance of the receiver. The other solution consists in designing the receiver with thin single mode waveguides, which reduces the propagation loss but also increases the complexity of the chip due to the requirement of polarization splitters and/or rotators. Figure 5.1 shows the simulation results of the electric fields of the TE_{00} and TM_{00} modes for two considered waveguide geometries.

5.2 Receiver based on a square 450 nm $\times$ 450 nm (width $\times$ thickness) waveguide

The receiver based on a square waveguide is the first to be explored in this thesis due to its simplicity. A polarization independent demultiplexer based on a square silicon nitride waveguide was demonstrated in the O-band [68]. In Paper [C] we propose a study of the mode effective area and polarization independence for different waveguide dimensions ranging from 300 nm (width) $\times$ 300 nm (thickness) to 800 nm (width) $\times$ 800 nm (thickness). To satisfy the single-mode behaviour, the waveguide needs to be smaller than 500 nm $\times$ 500 nm. The other aspect explored

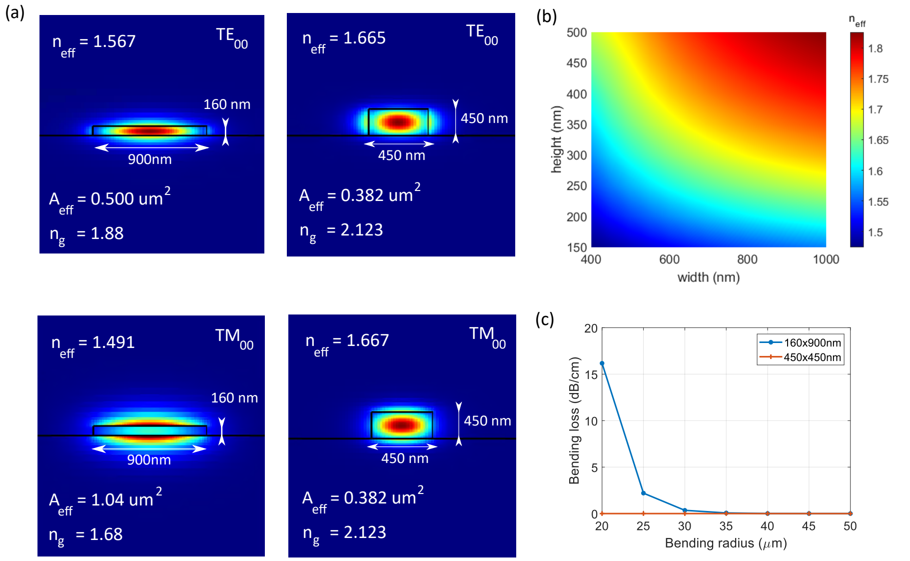

Figure 5.1: (a) Electric field of the TE_{00} and TM_{00} modes for the thin and thick waveguide. The FDE simulation results of the effective and group index (n_{eff} and n_g respectively) and of the mode effective area (A_{eff}) are also presented. (b) n_{eff} for different waveguide dimensions. (c) Simulation of the bending loss for both waveguides.

in Paper [C] is the coupling of the light from the single-mode fiber and the PIC. To avoid extra-loss due to polarization variations, we cannot use an inverse taper as for Paper [B]. Several fork- or trident-shaped designs have been demonstrated. A compact trident design based on Silicon assisted with gratings have also been proposed [99]. Paper [C] explores a similar model but based on silicon nitride. The total length of the proposed device is 300 μm-long and is adapted for packaging with a cleaved single-mode fiber (without a lens). The core diameter of the fiber is 5.3 μm, which results in a waist beam radius of approximately 6 μm at 1060 nm. The simulations are realized with 3D-FDTD where the fiber is also taken in account.

5.3 Receiver based on a thin 900 nm $\times$ 160 nm (width $\times$ thickness) waveguide

Reducing the mode confinement in a single-mode waveguide by selecting a square geometry increases the mode interaction with the sidewalls. Such waveguides have higher propagation loss as demonstrated in Refs [68,98] (30-190 dB/m) whereas propagation losses in photonic integrated circuits (PICs) lower than 4-6 dB/m are generally preferred. Such loss levels can be obtained by enlarging the waveguide as in Ref [98] and also by making it thinner as in Ref [48]. In Paper [D], we propose a receiver based on the original 900 nm $\times$ 160 nm (width $\times$ thickness) used in Paper [B]. Hence, unlike in Paper [C], the effective indices for TE and TM fundamental modes will differ. Therefore, additional components are necessary to achieve polarization independence, such as polarization splitters or polarization rotators.

Paper [D] proposes two receiver structures: one only using a polarization splitter and another combining a splitter with a rotator. A polarization splitter can be designed based on a simple directional coupler, with each output port assigned for one polarization. To rotate the polarization however, the device's structure needs to be asymmetric. Several design techniques have been successfully demonstrated such as partially etching the waveguide [100] or bi-layer [101, 102] or multimode sections [103, 104]. Several polarization independent receivers based on AWGs or cascaded MZIs are proposed in Refs [100, 105, 106].

An alternative than partially etching the waveguide to create a polarization rotator consists in depositing an additional layer above the waveguide. This second layer can be made of the same or another material. For example, in Ref [107] the main waveguide is made of silicon and the additional layer is made of silicon nitride. As the refractive index of silicon nitride is much smaller than silicon, the guided mode odes not transfer completely from the main silicon waveguide into the silicon nitride waveguide. To rotate the polarization, the silicon nitride waveguide moves away from the main silicon waveguide. In our case, the two layers would be made of silicon nitride. The main challenge would be controlling the thickness of the gap and the alignment between the two layers, which if not done properly, would decrease the device's performance. Hence, we selected in Paper [D] a design that requires partial etching as for Ref [100].

CHAPTER 6

Demultiplexing for dense wavelength-division multiplexing (DWDM) at 1.5 μm

This chapter presents the study of AWGs for DWDM at 1550 nm and expands the results of multilayer integration of silicon nitride (Si_3N_4) in Paper [E]. We propose an integrated combination of frequency combs as input laser sources with a WDM system at 1.55 μm. A frequency comb consists of a laser source for which the optical spectrum is made of narrow and phase-locked frequency lines [108]. In this chapter, we will mainly focus on the transmitter side of the optical interconnect.

6.1 Integrated transmitter

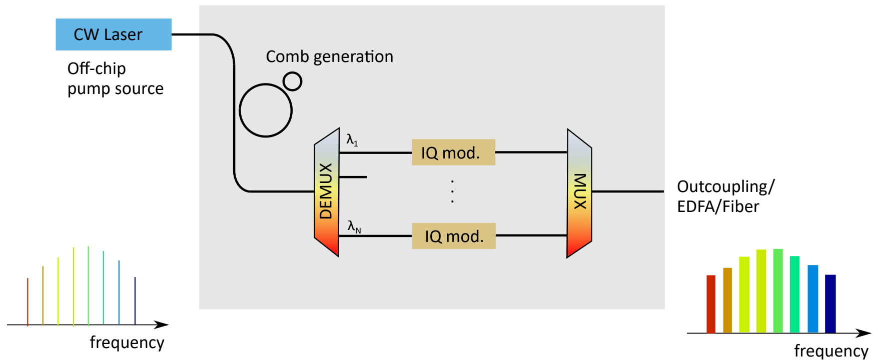

Figure 6.1: 1.55 μm interconnect: scheme of the multilayer chip.

Optical interconnects at 1.55 μm are used for fiber links that are several km-long and the power attenuation in single-mode fibers is around 0.2 dB/km [15] at this wavelength, which is negligible for links shorter than 1 km. However, after a certain propagation length (100 km), the loss becomes considerable and optical amplifiers are used to restore the optical power [109]. A common optical amplifier used for fiber communication is the erbium-doped amplifier fiber (EDFAs). To reach a desirable power, the fiber link becomes an N-repetition of a L-km fiber followed by an EDFA [108].

Paper [E] demonstrates a micro comb with approximately 50 comb lines above -20 dBm. If these 50 comb lines are later demultiplexed and modulated with quadrature amplitude modulation (QAM), then a capacity above several Tb/s could be achieved. Figure 6.1 illustrates the envisioned integrated transmitter for optical interconnects at 1.55 μm. The transmitter is based on a frequency comb source, which can be easily integrated in a photonic platform. Possible materials choices are $LiNbO_3$ [110], AlGaAsOI [111] and Si_3N_4 [112]. Among these materials, Si_3N_4 was selected for its ultra-low loss PICs, wide transparency window and compatibility with CMOS process. Moreover, to achieve conversion above 50%, an external ring is placed beside the main ring [113]. The other integrated elements are a demultiplexer to demultiplex the comb line frequencies and IQ modulators.

However, optical integration of all of these elements is not simple. Indeed, generation of solitons in the micro-comb required a dispersion engineered waveguide as explained in Paper [E]. In addition, the waveguide needs to be single-mode for the demultiplexer. An almost square single-mode 800 nm x 740 nm waveguide for example has a dispersion close to 0 and is more adapted for solitons generation. However, the imposed geometry considerably reduces the confinement of the propagating mode, thus increasing the interaction with the sidewalls. This is not suitable because roughness on the sidewalls will lead to high propagation loss in this case.

Therefore, selecting a width dimension of 1900 nm (while conserving the thickness of 740 nm) decreases the interaction between the guide mode and the sidewalls, hence reducing the propagation loss. This dispersion engineered waveguide is adapted for comb generation, but is also multimode, not suitable for the demultiplexers, which require single-mode behaviour. Thus, there is a tradeoff between mode confinement, propagation loss and single-mode behaviour. Therefore, designing a multilayer platform is a good tradeoff to meet all the requirements. Hence, the chip is designed as shown in Figure 6.2, with each layer designed for each specific component: a layer based on a 1900 nm (width) $\times$ 740 nm (thickness) waveguide for the micro-comb and a layer based on a 1500 nm (width) $\times$ 200 nm (thickness) waveguide for the demultiplexers. In addition, the transmitter is divided in two materials: Si_3N_4 layers for the comb and the demultiplexers and a $LiNbO_3$ layer for the modulators. Indeed, $LiNbO_3$ was the material selected for the modulators due to its low loss, modulation speed and driving voltage at 1550 nm [114, 115]. SOI IQ modulators were also demonstrated in the C- and L-band [116] as an alternative to $LiNbO_3$ to further reduce the cost and the footprint of the device. The thickness is 740 nm for the comb and 200 nm for the demultiplexers. This tradeoff then requires integration of 3D vertical coupling between the 740 nm and the 200 nm-thick layers. Paper [E] successfully demonstrates efficient coupling between the nonlinear platform (740 nm) and the linear platform (200 nm) with an insertion loss of 0.05 dB. However, this paper demonstrates only the first half of the designed chip (Comb and demultiplexer). Ref [117] demonstrates with simulations vertical coupling between a Si_3N_4 and a $LiNbO_3$ platform with a coupling loss of 0.08 dB.

Table 6.1 presents the estimated allowed loss for each component of the transmitter based on the target BER. The high estimated loss (10 dB) in the modulators is due to the fact that the optical power after modulation depends on the modulation format (4QAM, 16QAM,

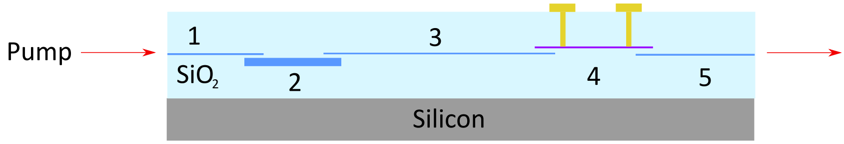

1: input waveguide, inverse taper (thin SiN layer)
2: comb generator (thick SiN layer)
3: 3dB splitter and DEMUX (thin SiN layer)
4: IQ modulator (Lithium Niobate layer)
5: MUX and out-coupling (thin SiN layer)

Figure 6.2: Scheme of the chip with the different layers.

64QAM). Therefore, the worst case scenario was preferably considered in our power budget.

Element	Loss	Power
Input CW		11 dBm
Coupling and 3 dB splitter	4 dB	7 dBm
Comb generation	approx 50% eff.	-13 dBm/ch
MUX (AWG)	$<$ 2 dB	-15 dBm/ch
Interlayer	$<$ 1 dB	-16 dBm/ch
Modulator array	$<$ 10 dB/modulator	-26 dBm/ch
Interlayer	$<$ 1 dB	-27 dBm/ch
DEMUX (AWG)	$<$ 2 dB	-29 dBm/ch
Coupling loss and PM (pol. rotation)	2 dB	-31 dBm/ch

Table 6.1: Power budget for each component.

6.2 Waveguide geometries

Two waveguide geometries were considered for the AWG in the linear layer: a 1000 nm x 200 nm and a 1500 nm x 200 nm waveguide. The Si_3N_4 waveguide is sandwiched between two SiO_2 cladding layers. The bottom SiO_2 cladding is thermally deposited on top a Silicon substrate. Then the linear layer of Si_3N_4 is deposited with LPCVD. Finally, a 3 μm-thick top LPCVD SiO_2 cladding is deposited.

6.3 Design and simulations of the AWGs

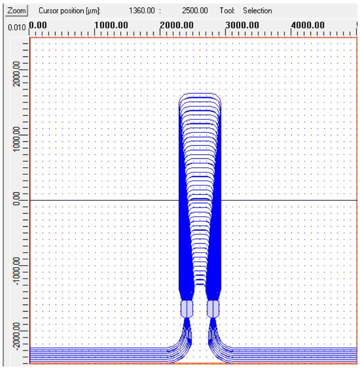

Figure 6.3: Device layout created from WDM PHASAR software.

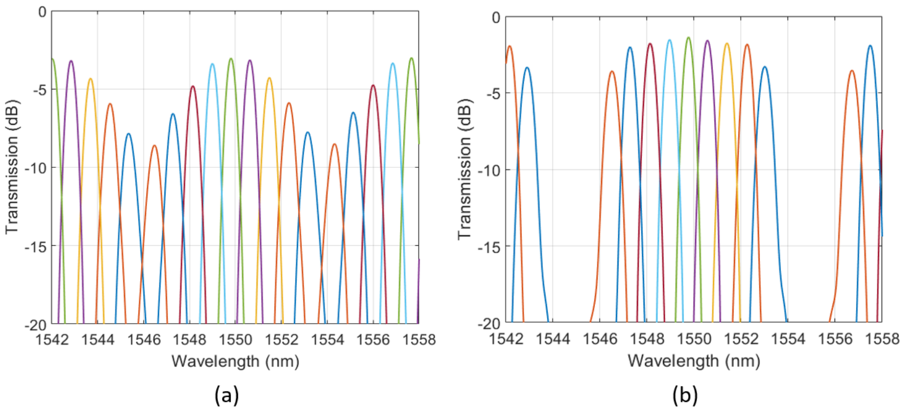

Figure 6.4: Simulations of AWGs with FSR of (a) 8 nm and (b) 10 nm.

Once the waveguide geometry and the main parameters of the AWG

AWG	FSR	Channel spacing	IL
w=1500 nm x h=200 nm	8 nm	0.8 nm	5.33 dB
w=1000 nm x h=200 nm	10 nm	0.8 nm	2.09 dB

Table 6.2: AWG simulation performances.

selected (length of the free propagation region, length increment, channel spacing, FSR), the component is drawn in the simulation tool as shown in Figure 6.3. The desired wavelength channel spacing here is 100 GHz (0.8 nm) due to the requirement of ultra-high channel count for combs [118]. Three different AWGs were designed based on the two waveguide geometries in the previous section. The first device is based on the 1500 nm x 200 nm with a designed FSR of 10 nm. However, the input and output channels were manually written to orient the device in the waveguide direction (see Figure 6.6). The second is based on the same waveguide geometry but with an FSR of 8 nm and the third based on the 1000 nm x 200 nm waveguide with an FSR of 10 nm. As the first device did not work during the measurements, only the simulations of the last two components are shown. Figure 6.4 presents the simulation of both devices for TE polarization. It can be noticed that the insertion loss of the 8 nm - FSR AWG is not uniform with respect to the second design (around 5 dB for the first AWG and 2 dB for the second). When comparing the designs, the separation between the receiver waveguides is the same but the free propagation region (FPR) length is smaller for the 8 nm - FSR AWG, which leads to a smaller Rowland circle. Therefore, the light from the arrayed waveguides is less focused on the outer channels, which results in the strong non-uniformity in the first design.

6.4 Manufacturing and testing the AWGs

AWG color	Waveguide	FSR
Blue	w=1500 nm x h=200 nm	9.75 nm
Green	w=1000 nm x h=200 nm	10 nm
Yellow	w=1500 nm x h=200 nm	7.83 nm

Table 6.3: Color code of the AWGs on the mask layout, each color indicating different FSRs and/or waveguide dimensions.

Figure 6.5 shows the mask layout of the testing chip with different as-

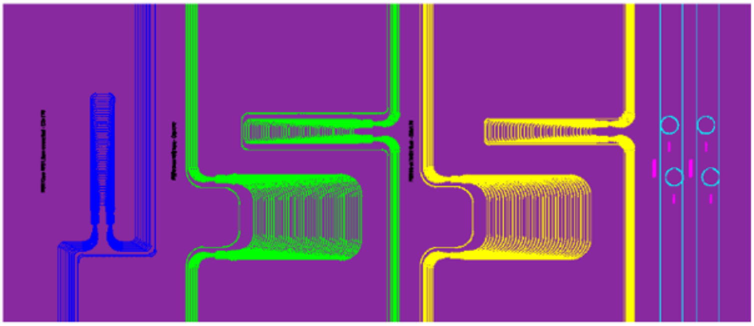

Figure 6.5: Mask layout of the chip. The distance between the FPRs for the small AWGs is 400 μm and is 4000 μm for the wide AWGs.

signed colors depending on their parameters (e.g. waveguide dimensions, designed FSR). AWGs with wider curved sections were also designed to reduce the radiation loss. Table 6.3 shows the main AWG parameters depending on the color. Reference waveguides are manufactured alongside the devices to identify the polarization (the TM polarization is more lossy than the TE polarization due to its weaker waveguide confinement) and to estimate the insertion loss of each channel. Figure 6.6a shows the device under test with the light coming from a laser emitting at 650 nm for initial alignments between the lensed fibers and the chip. The alignment is then optimized without the laser emitting in the visible range and is done with a power meter. Figure 6.6b shows the characterization of the AWG when the wavelength of the laser is swept between 1510 and 1620 nm. The blue continuous curve corresponds to the signal coming from the reference waveguide and the others from each channel of the AWG. 10 FSRs of the AWG are clearly visible and the average FSR measured is 9.5 nm for a target of 10 nm. Deviations in the fabrication such as the waveguide's refractive index or thickness can contribute to this deviation from the simulations.

Figure 6.7 presents the characterization results of the AWGs from the central input channel of both devices. Overall, the measurements are in agreement with simulations in terms of channel spacing, FSR, channel uniformity and insertion loss. The central channel remains difficult to control as it can be seen how far it deviates from 1550 nm in Figure 6.7. The measured average insertion loss is also lower from the simulations, which could be due to possible damage in the reference waveguide or

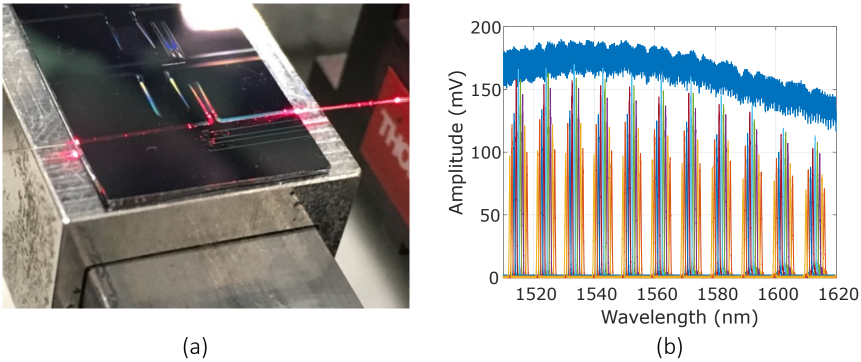

Figure 6.6: Characterization of an AWG based on a 1000 nm (width) x 200 nm (thickness) waveguide (a) Image of the measured chip with in/output coupling lensed fibers. (b) Wavelength sweeping of the tunable laser from 1510 to 1620 nm. The blue curve represents the measured output power from the reference waveguide. The measured peaks come from the 9 channels of the AWG. The measured FSR is approximatley 9.5 nm.

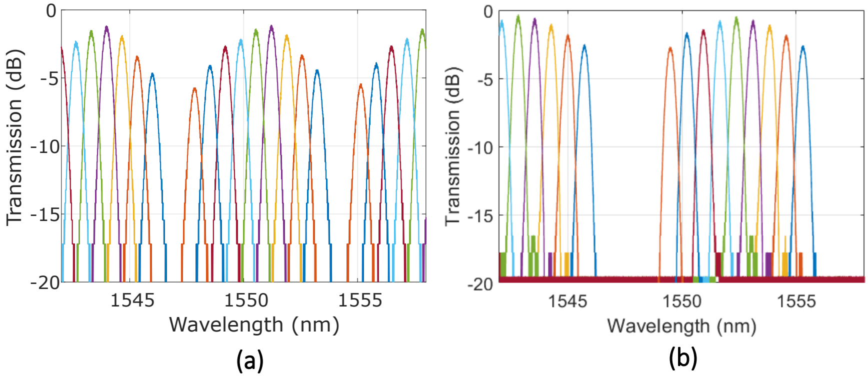

Figure 6.7: Characterization results of the AWGs. (a) DEMUX based on the 1500 nm x 200 nm waveguide with a designed FSR of 8nm. (b) DEMUX based on the 1000 nm x 200 nm waveguide with a designed FSR of 10 nm. The polarization state is TE.

to poor alignment between the lensed fibers and the taper's edge of the waveguide.

AWG	FSR	Channel spacing	IL
w=1500 nm x h=200 nm	7.23 nm	0.68 nm	3.0 dB
w=1000 nm x h=200 nm	9.57 nm	0.73 nm	1.49 dB

Table 6.4: AWG measured performances.

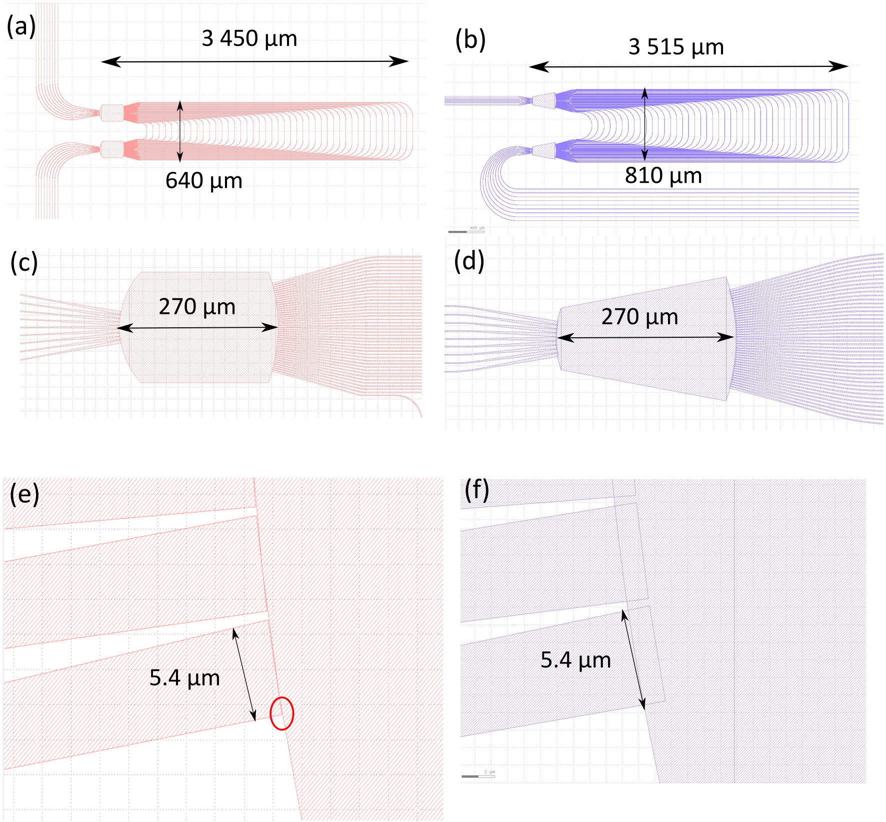

Figure 6.8: Comparison between the KLayouts of the (a), (c) and (e) AWG generated by the WDM PHASAR software and the (b), (d) and (f) AWG coded in Python. (a) and (b) Overall view of both devices. (c) and (d) Zoom at the first FPR. (e) and (f) Zoom at the receiver waveguides - FPR section. The red circle in (e) highlights a 26 nm wide gap between the taper and the FPR.

6.5 Enhanced AWG mask layout for the final PIC

The software used to simulate the AWG can also generate the mask layout for the fabrication. However, several issues with the generated design occur. The first one is that we cannot orient the receiver waveguides as we wish as shown in Figure 6.8a. Indeed, the in/output waveguides of the (de-)multiplexer are orientated in the normal direction to the arrayed waveguides and we want them in the parallel direction (see Figure 6.8b). This is to limit the stitching errors that may occur during the manufacturing process in one direction. Indeed, since the component is way too big to be patterned into a single E-beam writing field, it is divided in several writing fields that are 1024x1024 μm^2. Therefore, we wish to keep the spacing between the components as small as possible. The second problem with the mask created with the software is the gap count in the whole AWG. Indeed, many polygons do not perfectly coincide with each other, which create a multitude of gaps ranging from 1 nm between waveguide sections to sometimes 40 nm between tapers and the FPR section. Hence, we resorted to create a customized AWG software in Python to have more freedom in the design geometry. To minimize phase errors, the bending radius of the arrayed waveguides in the home-made AWG is kept the same (150 μm) with respect to the AWG generated by WDM PHASAR. The home-made AWG with Python shown in Figure 6.8b was later used for the PIC in Paper [E].

CHAPTER 7

Conclusions and future outlook

In this thesis I discussed flip-chip integration of a VCSEL over a PIC at 850nm, then presented an alternative integrated solution based on a Si_3N_4 PIC involving flip-chip of VCSELs and WDM at 1060 nm. I finally presented a multilayer approach at 1550 nm based on Si_3N_4. This chapter will highlight some areas that would need to be further developed in the future.

Paper [B] proposes a full PIC with flip-chip integrated VCSEL and photodetector. The VCSEL is single-mode and emits at 850 nm. The measured insertion losses were around 18 dB. The input grating coupler was a based on a staircase design whereas the output device was based on conventional design. In addition, the devices were not fully optimized and in future PICs involving VCSEL integration, the insertion loss could be reduced with a bottom DBR, BOX and cladding optimized thicknesses and finally with apodized grating couplers.

Papers [A], [C] and [D] treat of optical interconnects at 1 μm. In Paper [A] we focused the transmitter side, especially on demultiplexers. A flat-top cascaded MZI was succesfully demonstrated with experiments, but the device is limited by additional unwanted side-lobes. To reduce the level of the side-lobes, a more advanced design with additional stages and/or more advanced broadband power splitters would be required.

In Papers [C-D], we focused on the receiver side and propose solutions based on simulations. On the transmitter side, a 4-VCSEL array developed and then flip-chipped over a PIC that includes a flat-top cascaded MZI. On the receiver side, we could manufacture a PIC either based on square waveguides as proposed in Paper [C] or on thin waveguides as in Paper [D]. The advantage of square waveguides is the reduction of the complexity of the PIC, but at the cost of higher propagation loss and of polarization diversity in the event of fabrication deviations in the waveguide geometry. If this design is selected, then careful alignment between the SMF and the trident taper would be required. In addition, testing several grating trident tapers would be necessary to test the robustness of the design. If a receiver based on the designs proposed in Paper [D], the robustness of the polarization splitter-rotator. In addition, to see if the rotation of the polarization is succesful, grating couplers should be used at the input/output of the rotator, each designed for a different polarization state.

Finally, for the multilayer integration of SiN at 1550 nm, the full integrated transmitter which also includes a multiplexer and modulator arrays as described in Chapter 6 needs to be developed. In addition, to evaluate the AWG's crosstalk between two consecutive channels, a good idea for the next fabrication run would be for example designing for 1 test chip, 4 consecutive arrays without the modulator based on $LiNbO_3$ and the other 5 arrays with the modulator.

CHAPTER 8

Summary of papers

Paper A
Channel Scalability of Silicon Nitride (De-)multiplexers for Optical Interconnects at 1 μm
Journal of Lightwave Technology, 2023.
DOI: 10.1109/JLT.2023.3306478

We study the channel scalability for Arrayed Waveguide Gratings and cascaded MZIs at 1060nm. We compare the loss, crosstalk and footprint. 4-channel Gaussian AWG and Gaussian and flat-top MZI are also demonstrated. We then extrapolate the study to 8 and 16 channel with simulations. The study also compares Gaussian and Flat-top devices. The material of choice is silicon nitride for its low loss in the infrared and its good tradeoff between mode confinement (small devices) and sensitivity off effective index to waveguide core size (small phase errors).

My contribution: I designed all the components as well the mask design. I performed all the simulations and the measurements and wrote the whole paper. I was corresponding author and responded to the reviewer comments and added the modifications required.

Paper B
Angled Flip-Chip Integration of VCSELs on Silicon Photonic

Integrated Circuits

Journal of Lightwave Technology, Vol. 40, No. 15, pp. 5190-5200, August 1, 2022. DOI: 10.1109/JLT.2022.3172781

This article demonstrates a complete silicon photonic integrated circuit with a flip-chiped singlemode 850 nm VCSEL at the input and a photodiode (PD) at the output. We investigated the coupling efficiency of the grating couplers and the optical feedback on the VCSEL or in other words the amount of reflected light on the VCSEL aperture in the contra- and the codirectional configurations. The transmission is measured in different scenarios: VCSEL-PD, VCSEL-singlemode fiber and VCSEL-multimode fiber.

My contribution: I did all the simulations of the coupling efficiencies in every configuration (contra- and co-directional) for each VCSEL angle and dimension as well as the simulation of the optical feedback. I also wrote the second half of section II, all the section III and partially section IV. I also added the modifications required by the reviewers.

Paper C
Polarization-insensitive silicon nitride photonic receiver at 1 μm for optical interconnects

Submitted, 2023.

We design and simulate a polarization independent WDM receiver based on a square waveguide at 1 μm. We present a solution based on edge coupling and evaluate with simulations the propagation loss for different waveguide dimensions. A geometry of 450 nm $\times$ 450 nm is selected as a tradeoff between single-mode behaviour, low footprint and propagation loss.

My contribution: I designed all the components, realized most of the simulations and wrote the whole paper.

Paper D
Receiver platform based on thin silicon nitride waveguides at 1 μm

Submitted, 2023.

We design and simulate a polarization independent WDM receiver based on a thin waveguide at 1 μm. We present two solutions based on edge coupling. One consists in the use of a polarization splitter and an AWG and another with a polarization splitter-rotator followed by two cascaded MZIs, one for each polarization.

My contribution: I designed all the components and wrote the whole paper.

Paper E
Multilayer integration in silicon nitride: decoupling linear and nonlinear functionalities for ultralow loss photonic integrated systems
Optics Express, Vol. 31, No. 19, 11 Sep 2023.

We present a dual layer integrated photonic chip with two Silicon Nitride platforms with ultralow loss (a few dB/m) involving a comb source, demultiplexer and vertical coupler. The goal of the study is to overcome the tradeoff limitations between loss, mode confinement and multimode behaviour by integrating a nonlinear layer (micro-comb) and a linear layer (3 dB splitter, demultiplexer) in one chip. The mode transition between the nonlinear and linear platform is done with a 3D coupler. The material of choice is Silicon Nitride for its ultralow loss in a large wavelength range from visible to mid-infrared. The integration of these two individually optimized Silicon Nitride platforms could allow linear processing tasks of nonlinear Kerr applications.

My contribution: I designed the demultiplexing device, assisted the characterization of the chip when the AWG was involved and simulated with 3D-FDTD and EME the 3D-coupler.

References

[1] "https://www.itu.int/pub/r-rep-m.2370."

[2] F. Tariq, M. R. A. Khandaker, K.-K. Wong, M. A. Imran, M. Bennis, and M. Debbah, "A speculative study on 6G," *IEEE Wireless Communications*, vol. 27, no. 4, 2020.

[3] "https://digital-strategy.ec.europa.eu/en/library/energy-efficient-cloud-computing-technologies-and-policies-eco-friendly-cloud-market."

[4] statistica, "https://www.statista.com/statistics/633826/worldwide-hyperscale-data-center-numbers/."

[5] "https://www.rankred.com/largest-data-centers-in-the-world/."

[6] E. Simpanen, J. Gustavsson, E. Haglund, E. Haglund, A. Larsson, W. Sorin, S. Mathai, and M. Tan, "1060 nm single-mode vertical-cavity surface-emitting laser operating at 50 Gbit/s data rate," *Electronics letters*, vol. 53, no. 13, pp. 869–871, 2017.

[7] A. Larsson, E. Simpanen, J. Gustavsson, E. Haglund, E. Haglund, T. Lengyel, P. Andrekson, W. Sorin, S. Mathai, M. Tan, and S. Bickham, "1060 nm VCSELs for long-reach optical interconnects," *Elsevier Optical Fiber Technology*, vol. 44, pp. 36–42, 2018.

[8] X. Hu, M. Girardi, Z. Ye, P. Muñoz, A. Larsson, and V. Torres-Company, "Si3N4 photonic integration platform at 1 μm for optical

interconnect," *Optics Express*, vol. 28, no. 9, pp. 13 019–13 031, 2020.

[9] D. Mahgerefteh, C. Thompson, C. Cole, G. Denoyer, T. Nguyen, I. Lyubomirsky, C. Kocot, and J. Tatum, "Techno-economic comparison of silicon photonics and multimode VCSELs," *Journal of Lightwave Technology*, vol. 34, no. 2, pp. 233–242, 2016.

[10] R. P. J. M. Castro and, B. Kose, Y. Huang, B. Lane, K. Szczerba, P. Westbergh, T. Lengyel, J. S. Gustavsson, A. Larsson, and P. A. Andrekson, "50gb/s 4-PAM over 200m of high bandwidth MMF using a 850nm VCSEL," in *Optical Fiber Communication Conf.*, San Francisco, California, United States, 2014.

[11] T. Lengyel, K. Szczerba, E. P. Haglund, P. Westbergh, M. Karlsson, A. Larsson, and P. A. Andrekson, "Impact of damping on 50 Gbps 4-PAM modulation of 25g class VCSELs," *Journal of Lightwave Technology*, vol. 35, no. 19, 2017.

[12] M. Freebody, "Lasers evolve to meet the demands of optical communications," *Photonics spectra*, vol. 46, pp. 50–53, 2012.

[13] K. Szczerba, T. Lengyel, M. Karlsson, P. A. Andrekson, and A. Larsson, "94-Gb/s 4-PAM using an 850-nm VCSEL, pre-emphasis, and receiver equalization," *IEEE Photonics Technology Letters*, vol. 28, no. 22, 2016.

[14] P. Moser, J. A. Lott, P. Wolf, G. Larisch, H. Li, N. N. Ledentsov, and D. Bimberg, "Impact of the aperture diameter on the energy efficiency of oxide-confined 850 nm high-speed VCSELs," in *SPIE*, San Francisco, California, United States, 2013.

[15] M.-J. Li, "Novel optical fibers for data center applications," in *Proceedings of SPIE*, San Francisco, California, United States, 2016.

[16] S. Li, M. S. Nezami, S. Mishra, and O. Liboiron-Ladouceur, "Spectral-dependent electronic-photonic modeling of high-speed VCSEL-MMF links for optimized launch conditions," *Optics Express*, vol. 29, no. 2, pp. 2738–2756, 2021.

[17] M. Jahed, J. S. Gustavsson, and A. Larsson, "VCSEL wavelength setting by intra-cavity phase tuning - numerical analysis and experimental verification," *IEEE Journal of Quantum Electronics*, vol. 57, no. 6, pp. 1–7, 2021.

[18] T. Lengyel, E. Simpanen, J. Gustavson, A. Larsson, M. Karlsson, P. Andrekson, W. Sorin, S. Mathai, M. Tan, and S. Bickham, "Pre-emphasis enabled 50 gbit/s transmission over 1000 m smf using a 1060 nm single-mode VCSEL," *Electronics Letters*, vol. 54, no. 20, 2018.

[19] B. J. Puttnam, G. Rademacher, and R. S. Luís, "Space-division multiplexing for optical fiber communications," *Optica*, vol. 8, no. 9, 2021.

[20] S. S. Cheung and M. R. T. Tan, "Silicon nitride (Si3N4) (de-)multiplexers for 1-μm CWDM optical interconnects," *Journal of Lightwave Technology*, vol. 38, no. 13, pp. 3404–3413, 2020.

[21] X. Deng, F. Zhao, J. Zou, and R. T. Chen, "Passive single-mode wavelength-division (de)multiplexers for short- link multi-wavelength applications in field environments," in *SPIE*, 2001.

[22] J. Wang, Z. Sheng, and L. L. et al., "Low-loss and low-crosstalk 8 $\times$ 8 silicon nanowire AWG routers fabricated with CMOS technology," *Optics Express*, vol. 22, no. 8, 2014.

[23] Y. Sun, R. Lingle, and R. S. et al., "51.56 Gb/s SWDM PAM4 transmission over next generation wide band multimode optical fiber," in *OFC*, 2016.

[24] J. Lavrencik, S. Varughese, and V. A. T. et al., "2λ $\times$ 100Gbps PAM-4 Wideband Fiber 100m links using 850nm and 940nm VC-SELs," in *OFC*, 2016.

[25] J. A. Tatum, D. Gazula, and L. A. G. et al., "VCSEL-Based Interconnects for Current and Future Data Centers," *Journal of Lightwave Technology*, vol. 33, no. 4, pp. 727–732, 2015.

[26] IBM. Silicon photonics. [Online]. Available: https://www.zurich.ibm.com/st/photonics/optics.html

[27] N. Margalit, C. Xiang, S. M. Bowers, A. Bjorlin, R. Blum, and J. Bowers, "Perspective on the future of silicon photonics and electronics," *Applied Physics Letters*, vol. 118, no. 220501, 2021.

[28] W. Yang, Y. Li, and F. M. et al., "III-V comound materials and lasers on silicon," *Journal of Semiconductors*, vol. 40, no. 101305, 2019.

[29] Y. Hu, D. Liang, and K. M. et al., "III/V-on-Si MQW lasers by using a novel photonic integration method of regrowth on a bonding template," *Light: Science & Applications*, vol. 8, no. 93, 2019.

[30] H. Lu, J. S. Lee, Y. Zhao, C. Scarcella, P. Cardile, A. Daly, M. Ortsiefer, L. Carroll, and P. O'Brien, "Flip-chip integration of tilted VCSELs onto a silicon photonic integrated circuit," *Optics Express*, vol. 24, no. 15, 2016.

[31] Z. Zhou, B. Yin, and J. Michel, "On-chip light sources for silicon photonics," *Light: Science & Applications*, vol. 4, no. e358, 2015.

[32] S. Fathololoumi, D. Hui, and S. J. et al., "1.6 tbps silicon photonics integrated circuit and 800 gbps photonic engine for switch co-packaging demonstration," *Journal of Lightwave Technology*, vol. 39, no. 4, pp. 1155–1161, 2021.

[33] X. Chen, M. M. M. , and S. Stanković, "The emergence of silicon photonics as a flexible technology platform," *Proceedings of the IEEE*, vol. 106, no. 12, 2018.

[34] M. K. Smit and C. van Dam, "PHASAR-based WDM-devices: Principles, design and applications," *IEEE Journal of Selected topics in Quantum Electronics*, vol. 2, no. 2, pp. 236–250, 1996.

[35] P. Muñoz, D. Pastor, J. Capmany, and S. Sales, "Analytical and numerical analysis of phase and amplitude errors in the performance of arrayed waveguide gratings," *IEEE Journal of selected topics in quantum electronics*, vol. 8, no. 6, pp. 1130–1141, 2002.

[36] P. Muñoz, D. Pastor, and J. Capmany, "Modeling and design of arrayed waveguide gratings," *Journal of Lightwave Technology*, vol. 20, no. 4, pp. 661–674, 2002.

[37] E.-S. Kang, W.-S. Kim, D.-J. Kim, and B.-S. Bae, "Reducing the thermal dependence of silica-based arrayed-waveguide grating using inorganicâorganic hybrid materials," *IEEE Photonics Technology Letters*, vol. 16, no. 12, pp. 2626–2627, 2004.

[38] R. Baets, A. Z. Subramanian, S. Clemmen, B. Kuyken, P. Bienstman, N. L. Thomas, G. Roelkens, D. V. Thourhout, P. Helin, and S. Severi, "Silicon photonics: silicon nitride vs silicon-on-insulator," in *Optical Fiber Communications Conference and Exhibition (OFC)*, Anaheim, CA, USA, 2016.

[39] Y. Su, Y. Zhang, C. Qiu, X. Guo, and L. Sun, “Silicon photonic platform for passive waveguide devices: Materials, fabrication, and applications,” *Advanced Materials Technologies*, vol. 5, no. 8, 2020.

[40] J. Yota, “Effects of Deposition Method of PECVD Silicon Nitride as MIM Capacitor Dielectric for GaAs HBT Technology,” *ECS Transactions*, vol. 35, no. 229, 2011.

[41] T. Akiyama, S. Oda, Y. Nakasha, A. Hayakawa, S. Tanaka, Y. Tanaka, and T. Hoshida, “Cascaded AMZ triplets: a class of demultiplexers having a monitor and control scheme enabling dense WDM on Si nano-waveguide PICs with ultralow crosstalk and high spectral efficiency,” *Optics Express*, vol. 29, no. 6, pp. 7966–7985, 2021.

[42] L. Chrostowski and M. Hochberg, *Silicon Photonics Design.* Cambridge University Press, 2015.

[43] B. S. Ahluwalia, Ø. I. Helle, and O. G. Hellesø, “Rib waveguides for trapping and transport of particles,” *Optics Express*, vol. 24, no. 5, pp. 4477–4487, 2016.

[44] N. Eti and H. Kurt, “Model analysis of ridge and rib types of silicon waveguides with void compositions,” *IEEE Journal of Quantum Electronics*, vol. 52, no. 10, 2016.

[45] T. H. Talukdar, G. D. Allen, I. Kravchenko, and J. D. Ryckman, “Single-mode porous silicon waveguide interferometers with unity confinement factors for ultra-sensitive surface adlayer sensing,” *Optics Express*, vol. 27, no. 16, pp. 22 485–22 498, 2019.

[46] M. Zhang, G.Hu, S. Zhang, D. Gao, Y. Sun, and F. Wang, “Gain characteristics of the hybrid slot waveguide amplifiers integrated with NaYF4:Er3+ NPs-PMMA covalently linked nanocomposites,” *Royal society of chemistry*, vol. 10, no. 19, pp. 11 148–11 155, 2020.

[47] S. Roberts, X. Ji, J. Cardenas, M. Corato-Zanarella, and M. Lipson, “Measurements and modeling of atomic-scale sidewall roughness and losses in integrated photonic devices,” *Advanced Optical Materials*, no. 2102073, 2022.

[48] J. F. Bauters, M. J. R. Heck, D. John, D. Dai, M.-C. Tien, J. S. Barton, A. Leinse, R. G. Heideman, D. J. Blumenthal, and J. E.

Bowers, “Ultra-low-loss high-aspect-ratio (Si3N4) waveguides,” *Optics Express*, vol. 19, no. 4, pp. 3163–3174, 2011.

[49] *www.lumerical.com/learn/whitepapers/lumericals-2-5d-fdtd-propagation-method/.*

[50] A. Larsson, J. S. Gustavsson, E. Haglund, E. P. Haglund, E. Simpanen, and T. Lengyel, “VCSEL modulation speed: status and prospects,” in *Proceedings of SPIE*, San Francisco, California, United States, 2019.

[51] P. Westbergh, J. S. Gustavsson, A. Larsson, T. F. Taunay, L. Bansal, and L. Grüner-Nielsen, “Crosstalk characteristics and performance of VCSEL array for multicore fiber interconnects,” *IEEE Journal of Selected Topics in Quantum Electronics*, vol. 21, no. 6, pp. 429–435, 2015.

[52] D. L. Butler, M.-J. Li, S. Li, Y. Geng, R. R. Khrapko, R. A. Modavis, V. N. Nazarov, and A. V. Koklyushkin, “Space division multiplexing in short reach optical interconnects,” *Journal of Lightwave Technology*, vol. 35, no. 4, pp. 677–682, 2017.

[53] E. Haglund, M. Jahed, J. S. Gustavsson, A. Larsson, J. Goyvaerts, R. Baets, G. Roelkens, M. Rensing, and P. O´Brien, “High-power single transverse and polarization mode vcsel for silicon photonics integration,” *Optics Express*, vol. 27, no. 13, pp. 18 892–18 899, 2019.

[54] R. Soref, “Mid-infrared photonics in silicon and germanium,” *Nature Photonics*, vol. 4, no. 8, pp. 495–497, 2010.

[55] A. Z. Subramanian, P. Neutens, A. Dhakal, R. Jansen, T. Claes, X. Rottenberg, F. Peyskens, S. Selvaraja, P. Helin, P. D. Bois, K. Leyssens, S. Severi, P. Deshpande, R. Baets, and P. V. Dorpe, “Low-loss singlemode PECVD silicon nitride photonic wire waveguides for 532â900 nm wavelength window fabricated within a CMOS pilot line,” *IEEE Photonics Journal*, vol. 5, no. 6, 2013.

[56] M. I. Basudewa, Z. H. Bagaskara, S. S. A. Damita, R. F. Putra, and D. Ahmadi, “Bit error rate performance analysis for free space optic communication,” in *IOP Conference Series: Materials Science and Engineering*, 2020.

[57] N. Ismail, F. Sun, G. Sengo, K. Wörhoff, A. Driessen, R. M. de Ridder, and M. Pollnau, "Improved arrayed-waveguide-grating layout avoiding systematic phase errors," *Optics Express*, vol. 19, no. 9, pp. 8781–8794, 2011.

[58] R. Marz, "Dense wavelength division multiplex: Research activities at siemens," in *Proceedings of SPIE*, Beijing, China, 1996.

[59] Y. Hibino, "Recent advances in high-density and large-scale AWG multi/demultiplexers with higher index-contrast silica-based PLCs," *IEEE Journal of Selected Topics of Quantum Electronics*, vol. 8, no. 6, pp. 1090–1101, 2002.

[60] D. Dai and J. E. Bowers, "Silicon-based on chip multiplexing technologies and devices for peta-bit optical interconnects," *Nanophotonics de Gruyter*, vol. 3, no. 4-5, pp. 283–311, 2013.

[61] P. Pan, J. An, J. Zhang, Y. Wang, H. Wang, L. Wang, X. Yin, Y. Wu, J. Li, Q. Han, and X. Hu, "Flat-top awg based on inp deep ridge waveguide," *Elsevier Optical Communications*, vol. 255, pp. 376–381, 2015.

[62] A. A. Bernussi, L. G. de Peralta, V. Gorbounov, J. A. Linn, S. Frisbie, R. Gale, and H. Temkin, "Mirror quality and the performance of reflective arrayed-waveguide grating multiplexers," *Journal of Lightwave Technology*, vol. 22, no. 7, pp. 1828–1832, 2004.

[63] D. Dai and S. He, "Compact silicon-based wavelength-selective photonic integrated devices and the applications," in *Proceedings of SPIE*, San Jose, California, United States, 2009.

[64] W. Bogaerts, S. K. Selvaraja, P. Dumon, J. Brouckaert, K. D. Vos, D. V. Thourhout, and R. Baets, "Silicon-on-insulator spectral filters fabricated with cmos technology," *Journal of Selected Topics in Quantum Electronics*, vol. 16, no. 1, pp. 33–44, 2010.

[65] J.-J. He, B. Lamontage, A. Delâge, L. Erickson, M. Davies, and E. S. Koteles, "Monolithic integrated wavelength demultiplexer based on a waveguide rowland circle grating in InGaAsP/InP," *Journal of Lightwave Technology*, vol. 16, no. 4, pp. 631–638, 1998.

[66] F. Horst, W. M. J. Green, S. Assefa, S. M. Shank, Y. A. Vlasov, and B. J. Offrein, "Cascaded mach-zehnder wavelength filters

in silicon photonics for low loss and flat pass-band WDM (de-)multiplexing," *Optics Express*, vol. 21, no. 10, pp. 11 652–11 658, 2013.

[67] H. Xu and Y. Shi, "Flat-top CWDM (de)multiplexer based on MZI with bent directional couplers," *IEEE Photonics Technology Letters*, vol. 30, no. 2, 2018.

[68] J. C. Mikkelsen, A. Bois, T. Lordello, D. Mahgerefteh, S. Menezo, and J. K. S. Poon, "Polarization-insensitive silicon nitride Mach-Zehnder lattice wavelength demultiplexers for CWDM in the O-band," *Optics Express*, vol. 26, no. 23, pp. 30 076–30 084, 2018.

[69] D. Liu, M. Zhanh, Y. Shi, and D. Dai, "Four-channel CWDM (de)multiplexers using cascaded multimode waveguide gratings," *IEEE Photonics Technology Letters*, vol. 32, no. 4, 2020.

[70] D. Liu, H. Wu, and D. Dai, "Silicon multimode waveguide grating filter at 2 μm," *Journal of Lightwave Technology*, vol. 37, no. 10, pp. 2217–2222, 2019.

[71] Y. Tang, H. Wu, S. Wang, C. Li, and D. Dai, "Silicon-based hybrid demultiplexer for wavelength- and mode-division multiplexing," *Optics Letters*, vol. 43, no. 9, pp. 1962–1965, 2018.

[72] P. Chen, S. Chen, X. Guan, Y. Shi, and D. Dai, "High-order microring resonators with bent couplers for a box-like filter response," *Optics Letters*, vol. 39, no. 21, pp. 6304–6307, 2014.

[73] F. Xia, M. Rooks, L. Sekaric, and Y. Vlasov, "Ultra-compact high order ring resonator filters using submicron silicon photonic wires for on chip optical interconnect," *Optics Express*, vol. 15, no. 19, pp. 11 934–11 941, 2007.

[74] M. Cherchi, F. Sun, M. Kapulainen, M. Harjanne, and T. Aalto, "Flat-top interleavers based on single mmis," in *SPIE OPTO*, San Francisco, California, United States, 2020.

[75] G. Singh, A. Singh, R. P. Yadav, and V. Janyani, "Design and analysis of low loss MMI based 4x4 optical switch using benes architecture with SOAs," *2008 IEEE PhotonicsGlobal@Singapore*, 2008.

[76] G. F. R. Chen, J. R. Ong, T. Y. L. Ang, S. T. Lim, C. E. Png, and D. T. H. Tan, "Broadband silicon-on-insulator directional couplers using a combination of straight and curved waveguide sections," *Scientific Report*, vol. 7, no. 1, 2017.

[77] Y. Hibino, "Recent advances in high-density and large-scale AWG multi/demultiplexers with higher index-contrast silica-based PLCs," *IEEE Journal of Selected Topics in Quantum Electronics*, vol. 8, no. 6, pp. 1090–1101, 2002.

[78] F. Horst, W. M. J. Green, S. Assefa, S. M. Shank, Y. A. Vlasov, and B. J. Offrein, "Cascaded Mach-Zehnder wavelength filters in silicon photonics for low loss and flat pass-band WDM (de-)multiplexing," *Optics Express*, vol. 21, no. 10, pp. 11 652–11 658, 2013.

[79] A. Sure, T. Dillon, J. Murakowski, C. Lin, D. Pustai, and D. W. Prather, "Fabrication and characterization of three-dimensional silicon tapers," *Optics Express*, vol. 11, no. 26, pp. 3555–3561, 2003.

[80] G. Roelkens, D. V. Thourhout, and R. Baets, "High efficiency silicon-on-insulator grating coupler based on a poly-silicon overlay," *Optics Express*, vol. 14, no. 24, pp. 11 622–11 630, 2006.

[81] L. Cheng, S. Mao, Z. Li, Y. Han, and H. Y. Fu, "Grating couplers on silicon photonics: Design principles, emerging trends and practical issues," *MPDI Micromachines*, vol. 11, no. 666, 2020.

[82] S. Nambiar, P. Sethi, and S. K. Selvaraja, "Grating-assisted fiber to chip coupling for SOI photonic circuits," *MPDI Applied Sciences*, vol. 8, no. 1142, 2018.

[83] D. Marris-Morini, X. L. Roux, L. Vivien, E. Cassan, D. Pascal, M. Halbwax, S. Maine, and S. Laval, "Optical modulation by carrier depletion in a silicon pin diode," *Optics Express*, vol. 14, no. 22, pp. 10 838–10 843, 2006.

[84] G. Maire, L. Vivien, G. Sattler, A. Kaźmierczak, B. Sanchez, K. B. Gylfason, A. Griol, D. Marris-Morini, E. Cassan, D. Giannone, H. Sohlström, and D. Hill, "High efficiency silicon nitride surface grating couplers," *Optics Express*, vol. 16, no. 1, pp. 328–333, 2008.

[85] Y. Wang, H. Yun, Z. Lu, R. Bojko, W. Shi, X. Wang, J. Flueckiger, F. Zhang, M. Caverley, N. A. F. Jaeger, and L. Chrostowski, "Apodized focusing fully etched subwavelength grating couplers," *IEEE Photonics Journal*, vol. 7, no. 3, 2015.

[86] N. V. Sapra, D. Vercruysse, L. Su, K. Y. Yang, J. Skarda, A. Y. Piggott, and J. Vučković, "Inverse design and demonstration of broadband grating couplers," *IEEE Journal of Selected Topics in Quantum Electronics*, vol. 25, no. 3, pp. 1–7, 2019.

[87] J. Hong, A. M. Spring, F. Qiu, and S. Yokoyama, "A high efficiency silicon nitride waveguide grating coupler with a multilayer bottom reflector," *Scientific Reports*, vol. 9, no. 12988, 2019.

[88] D. Vermeulen, S. Selvaraja, P. Verheyen, G. Lepage, W. Bogaerts, P. Absil, D. V. Thourhout, and G. Roelens, "High-efficiency fiber-to-chip grating couplers realized using an advanced cmos-compatible silicon-on-insulator platform," *Optics Express*, vol. 18, no. 17, pp. 18 278–18 283, 2010.

[89] Y. Chen, R. Halir, I. Molina-Fernańdez, P. Cheben, and J.-J. He, "High-efficiency apodized-imaging chip-fiber grating coupler for silicon nitride waveguides," *Optics Letters*, vol. 41, no. 21, pp. 5059–5062, 2016.

[90] Y. Chen, T. Bucio, A. Z. Khokhar, M. Banakar, K. Grabska, F. Y. Gardes, R. Halir, I. Molina-Fernańdez, P. Cheben, and J.-J. He, "Experimental demonstration of an apodized-imaging chip-fiber grating coupler for Si3N4 waveguides," *Optics Letters*, vol. 42, no. 18, pp. 3566–3569, 2017.

[91] Y. Fei, T. Ye, W. Tang, and T. Chu, "Efficient adiabatic silicon-on-insulator waveguide taper," *Photon. Res.*, vol. 2, no. 3, 2014.

[92] P. Sethi, A. Haldar, and S. K. Selvaraja, "Ultra-compact low-loss broadband waveguide taper in silicon-on-insulator," *Optics Express*, vol. 25, no. 9, pp. 10 196–10 203, 2017.

[93] F. V. Laere, W. Bogaerts, D. V. T. D. Taillaert, P. Dumon, and R. Baets, "Compact focusing grating couplers between optical fibers and silicon-on-insulator photonic wire waveguides," in *Optical Fiber Communications Conference and Exhibition (OFC)*, Anaheim, CA, USA, 2007.

[94] F. V. Laere, W. Bogaerts, P. Dumon, G. Roelkens, D. V. Thourhout, and R. Baets, “Focusing polarization diversity grating couplers in silicon-on-insulator,” *Journal of Lightwave Technology*, vol. 27, no. 5, 2009.

[95] J. Zou, Y. Yu, M. Ye, L. Liu, S. Deng, and X. Zhang, “Ultra efficient silicon nitride grating coupler with bottom grating reflector,” *Optics Express*, vol. 23, no. 20, 2015.

[96] C.-C. Lin, Y.-C. L. Y.-H. Liu, L. Wang, and N. Na, “Design of a completely vertical, polarization-independent two-dimensional grating coupler with high coupling efficiency,” *MPDI Sensors*, vol. 23, no. 4662, 2023.

[97] T. Watanabe, Y. Fedoryshyn, and J. Leuthold, “2-d grating couplers for vertical fiber coupling in two polarizations,” *IEEE Photonics Journal*, vol. 11, no. 4, 2019.

[98] M. Girardi, A. Larsson, and V. Torres-Company, “Performance tradeoffs in low-loss Si3N4 waveguides for linear and nonlinear applications,” in *European Conference on Integrated Optics*, Milano, Italy, 2022.

[99] A. He, X. Guo, T. Wang, and Y. Su, “Ultracompact fiber-to-chip metamaterial edge coupler,” *ACS Photonics*, vol. 8, no. 11, p. 3226â3233, 2021.

[100] S. Guerber, C. A. Alonso-Ramos, X. L. Roux, N. Vulliet, E. Cassan, D. Marris-Morini, F. Boeuf, and L. Vivien, “Polarization independent and temperature tolerant AWG based on a silicon nitride platform,” *Optics Letters*, vol. 45, no. 23, pp. 6559–6562, 2020.

[101] H. Zhang, S. Das, J. Zhang, Y. Huang, C. Li, S. Chen, H. Zhou, M. Yu, P. G.-Q. Lo, and J. T. L. Thong, “Efficient and broadband polarization rotator using horizontal slot waveguide for silicon photonics,” *Applied Physics Letters*, vol. 101, no. 021105, 2012.

[102] B. Troia, F. D. Leonardis, M. Lanzafame, T. Muciaccia, G. Grasso, G. Giannoccaro, C. E. Campanella, and V. M. N. Passaro, “Design and optimization of polarization splitting and rotating devices in silicon-on-insulator technology,” *Advances in OptoElectronics*, 2014.

[103] Y. Zhang, Y. He, X. Jiang, B. Liu, C. Qiu, Y. Su, and R. A. Soref, "Ultra-compact and highly efficient silicon polarization splitter and rotator," *APL Photonics*, vol. 1, no. 091304, 2016.

[104] D. Dai and J. Bowers, "Novel concept for ultracompact polarization splitter-rotator based on silicon nanowires," *Optics Express*, vol. 19, no. 11, 2011.

[105] Q. Han, J. St-Yves, Y. Chen, M. Ménard, and W. Shi, "Polarization-insensitive silicon nitride arrayed waveguide grating," *Optics Letters*, vol. 44, no. 16, pp. 3976–3979, 2019.

[106] H. Xu, L. Liu, and Y. Shi, "Polarization-insensitive four-channel coarse wavelength-division (de)multiplexer based on Mach Zehnder interferometers with bent directional couplers and polarization rotators," *Optics Letters*, vol. 43, no. 7, 2018.

[107] P. Dong, Y.-K. Chen, G.-H. Duan, and D. T. Neilson, "Silicon photonic devices and integrated circuits," *De Gruyter*, vol. 3, no. 4-5, 2014.

[108] V. Torres-Company, J. Schröder, A. Fülöp, M. Mazur, L. Lundberg, Ó. B. Helgason, M. Karlsson, and P. A. Andrekson, "Laser frequency combs for coherent optical communications," *Journal of Lightwave Technology*, vol. 37, no. 7, pp. 1663–1670, 2019.

[109] W. Shieh and I. Djordjevic, *OFDM for Optical Communications*. Elsevier, 2010.

[110] Y. Gao, F. Lei, M. Girardi, Z. Ye, R. V. Laer, V. Torres-Company, and J. Schröder, "Compact lithium niobate microring resonators in the ultra-high-Q/V regime," *Optics Letters*, vol. 48, no. 15, 2023.

[111] H. Shu, L. Chang, Y. Tao, B. Shen, W. Xie, M. Jin, A. Netherton, Z. Tao, X. Zhang, R. Chen, B. Bai, J. Qin, S. Yu, X. Wang, and J. E. Bowers, "Microcomb-driven silicon photonic systems," *Nature*, vol. 605, pp. 457–463, 2022.

[112] X. Chen, S. Sun, W. Ji, X. Ding, Y. Gao, T. Liu, J. Wen, H. Guo, and T. Wang, "Soliton Microcomb on Chip Integrated Si3N4 Microresonators with Power Amplification in Erbium-Doped Optical Mono-Core Fiber," *MDPI micromachines*, vol. 13, no. 2125, 2022.

[113] Ó. B. Helgason, M. Girardi, Z. Ye, F. Lei, J. Schröder, and V. Torres-Company, “Surpassing the nonlinear conversion efficiency of soliton microcombs,” *Nature Photonics*.

[114] D. Zhu, L. Shao, and M. Y. et al., “Integrated photonics on thin-film lithium niobate,” *Advances in Optics and Photonics*, vol. 13, no. 2, 2021.

[115] Y. Li, T. Lan, D. Yang, J. Bao, M. Xiang, F. Yang, and Z. Wang, “High-performance Mach-Zehnder Modulator Based on Thin-Film Lithium Niobate with low voltage-length product,” *ACS Omega*, vol. 8, no. 10, 2023.

[116] K. Goi, A. Oka, and H. K. et al., “Low-loss high-speed silicon IQ modulator for QPSK/DQPSK in C and L bands,” *Optics Express*, vol. 22, no. 9, 2014.

[117] A. S. Alam, M. Girardi, A. Caut, A. Larsson, V. Torres-Company, M. Galili, Y. Ding, and K. Yvind, “LiNbO3/Si3N4-Bilayer Vertical Coupler for Integrated Photonics,” in *CLEO OSA*, 2020.

[118] P. M.-P. et al, “Microresonator-based solitons for massively parallel coherent optical communications,” *Nature*, vol. 546, no. 7657, pp. 274–279, 2017.

Included papers A–E

Paper A

"Channel Scalability of Silicon Nitride (De-)multiplexers for Optical Interconnects at 1 μm",
Alexander Caut, Marcello Girardi, Victor Torres-Company, Anders Larsson, and Magnus Karlsson,
Journal of Lightwave Technology, 2023.
DOI: 10.1109/JLT.2023.3306478

Paper B

"Angled Flip-Chip Integration of VCSELs on Silicon Photonic Integrated Circuits",
Mehdi Jahed, **Alexander Caut**, Jeroen Goyvaerts, Marc Rensing, Magnus Karlsson, Anders Larsson, Gunther Roelkens, Roel Baets, and Peter O'Brien,
Journal of Lightwave Technology, Vol. 40, No. 15, pp. 5190-5200, August 1, 2022, DOI: 10.1109/JLT.2022.3172781.

Paper C

“Polarization-insensitive silicon nitride photonic receiver at 1 μm for optical interconnects”,
Alexander Caut, Vijay Shekhawat, Victor Torres-Company, and Magnus Karlsson, *Submitted*, 2023.

Paper D

"Receiver platform based on thin Silicon Nitride waveguides at 1 μm",
Alexander Caut, Victor Torres-Company, and Magnus Karlsson, *Submitted*, 2023.

Paper E

"Multilayer integration in silicon nitride: decoupling linear and nonlinear functionalities for ultralow loss photonic integrated systems",
Marcello Girardi, Òskar B. Helgason, **Alexander Caut**, Magnus Karlsson, Anders Larsson, and Victor Torres-Company,
Optics Express, Vol. 31, No. 19, 11 Sep 2023.